**Title**: Protective mitochondrial fission induced by stress responsive protein GJA1-20k

**Authors**

Daisuke Shimura[1], Esther Nuebel[2,3,4], Rachel Baum[1], Shaohua Xiao[5], Junco S. Warren[1], TingTing Hong[1,6,7], Jared Rutter[2,3,6] & Robin M. Shaw[1,*]

**Affiliations**

1, Nora Eccles Harrison Cardiovascular Research and Training Institute, University of Utah, Salt Lake City, UT, USA.

2, Howard Hughes Medical Institute, University of Utah, Salt Lake City, UT, USA.

3, Department of Biochemistry, University of Utah, Salt Lake City, UT, USA.

4, Biomedical Sciences, Noorda College of Osteopathic Medicine, Provo, UT, USA

5, Department of Neurology, University of California at Los Angeles, Los Angeles, CA, USA.

6, Diabetes and Metabolism Research Center, University of Utah, Salt Lake City, UT, USA.

7, Department of Pharmacology and Toxicology, College of Pharmacy, University of Utah, Salt Lake City, UT, USA.

*Correspondence: Robin.Shaw@hsc.utah.edu

## Abstract

The Connexin43 gap junction gene *GJA1* has one coding exon, but its mRNA undergoes internal translation to generate N-terminal truncated isoforms of Connexin43 with the predominant isoform being only 20 kDa in size (GJA1-20k). Endogenous GJA1-20k protein is not membrane bound, and has been found to increase in response to ischemic stress, localize to mitochondria, and mimic ischemic preconditioning protection in the heart. However, it is not known how GJA1-20k benefits mitochondria to provide this protection. Here, we identify that GJA1-20k polymerizes actin around mitochondria which induces focal constriction sites. Mitochondrial fission events occur within about 45 seconds of GJA1-20k recruitment of actin. Interestingly, GJA1-20k mediated fission is independent of canonical Dynamin Related Protein 1 (DRP1). We find that GJA1-20k induced smaller mitochondria have decreased reactive oxygen species (ROS) generation and, in hearts, provide potent protection against ischemia-reperfusion injury. The results indicate that stress responsive internally translated GJA1-20k stabilizes polymerized actin filaments to stimulate non-canonical mitochondrial fission which limits ischemic-reperfusion induced myocardial infarction.

## Introduction

Ischemia-Reperfusion (I/R) injury is known to induce excessive reactive oxygen species (ROS) in mitochondria, which results in cellular dysfunction and organ damage. Interestingly, the phenomenon of ischemic preconditioning, first described thirty-five years ago (Murry et al., 1986), is a potent yet ironic protection of organs from ischemia-induced damage achieved by preceding the full ischemic insult with shorter bouts of ischemia. Despite the large therapeutic potential of preconditioning for any organ such as heart, kidney, skeletal muscle, or brain subjected to anticipated ischemia, the mechanisms of preconditioning are not well understood, nor has an intervention been identified to successfully translate the phenomenon into clinical utility (Heusch and Gersh, 2020).

Related to preconditioning is the perplexing dynamic regulation of mitochondria itself. Mitochondria undergo both fission and fusion in an adaptive equilibrium which directly affects cellular activity and response to stress s(Friedman and Nunnari, 2014, Youle and van der Bliek, 2012). It is not clear if an overall shift to fission or fusion is sufficient to define mitochondrial fidelity, or whether a change in the fission-fusion equilibrium occurs secondary to multiple distinct pathways which could be either beneficial or harmful, depending on the pathway taken. For instance, is mitochondrial fission a causative element of ROS generation, apoptosis, cellular senescence, and cell death (Nishimura et al., 2018, Suen et al., 2008, Wang et al., 2017), or is fission actually protective, such as by promoting mitophagy which can promote survival (Shirakabe et al., 2016, Burman et al., 2017)? The nuance in understanding the context of mitochondrial fission helps explain the complex relationship between mitochondrial morphology and function (Picard et al., 2013, Song et al., 2015, Nunnari and Suomalainen, 2012). If we have a better understanding of conditions in which mitochondrial fission results from a protective

mechanism, we will be closer to learning how to preserve mitochondrial fidelity in the setting of ischemic and reperfusion stress.

Both the gap junction protein Connexin43 (Cx43) and mitochondria are associated with preconditioning protection (Basheer et al., 2018, Rodriguez-Sinovas et al., 2018, Garcia-Dorado et al., 2006). Little is known how the gap junction channel and organelle convey protection during preconditioning. *GJA1*, which encodes Cx43, has a single coding exon and thus is not subject to splicing (Smyth and Shaw, 2013). However, *GJA1* mRNA is subject to endogenous internal translation generating several N-terminal truncated isoforms (Smyth and Shaw, 2013, Salat-Canela et al., 2014, Ul-Hussain et al., 2014). GJA1-20k, which contains the full Cx43 C-terminus but lacks transmembrane domains, is the most abundant and most common smaller isoform and is essential to full length Cx43 trafficking (Smyth and Shaw, 2013, Xiao et al., 2020) by recruiting cytoplasmic actin to organize trafficking pathways (Basheer et al., 2017). In addition, GJA1-20k is highly enriched at the outer mitochondrial membrane (Fu et al., 2017, Basheer et al., 2018). GJA1-20k abundance increases with hypoxic and ischemic stress(Basheer et al., 2018), resulting in a phenotypically profound cardiac protection that mimics ischemic preconditioning (Basheer et al., 2018, Wang et al., 2019). It is not known how GJA1-20k protects mitochondria during stress.

In the present study, we found an inverse relationship between the presence of GJA1-20k and mitochondria size in cultured cells and mice. This relationship is not affected by typical mediators of mitochondrial dynamics by Dynamin Related Protein 1 (DRP1), but rather is strongly dependent on actin dynamics. With the generation of smaller actin-associated mitochondria, we observed decreased oxygen consumption, decreased ROS generation, and profound protection against ischemia-reperfusion damage. Our data demonstrate a novel non-

canonical mechanism of protective mitochondrial fission which is dependent on GJA1-20k and cytoskeletal dynamics. The findings also identify GJA1-20k as a pharmaceutical candidate for protection of organs undergoing anticipated ischemia.

## Results

### GJA1-20k induces mitochondrial fission in vitro and in vivo

To understand the interplay between GJA1-20k and mitochondria, we expressed GJA1-20k in HEK293 cells and analyzed mitochondrial morphology by fluorescence imaging. GJA1-20k co-localizes with mitochondria and its presence results in a more rounded and punctate appearance of the mitochondria. GJA1-20k also induces a 54% decrease in average mitochondrial area (Figure 1A, F). siRNA-mediated knock-down of *GJA1* expression (Figure 1—figure supplement 1A) conversely increases mitochondrial area by 20% (Figure 1B, F). Furthermore, mitochondrial size after *GJA1* knock-down can be rescued by siRNA resistant GJA1-20k overexpression, but not with overexpression of siRNA resistant Cx43-M6L, which expresses full-length Cx43 without the truncated isoforms (Smyth and Shaw, 2013) (Figure 1—figure supplement 1B, C). Together, these data suggest that the short GJA1-20k isoform, but not full-length Cx43, reduces mitochondrial size.

Since GJA1-20k is abundantly expressed in cardiomyocytes (CMs) suggesting an important function in heart (Xiao et al., 2020, Smyth and Shaw, 2013), and GJA1-20k can convey ischemic preconditioning protection in heart (Basheer et al., 2018) we used cardiomyocytes as a primary cell model to explore GJA1-20k function. We overexpressed GJA1-20k by adenovirus transduction in wild type (WT) neonatal mouse CMs and found a decrease in the average mitochondria area (Figure 1C, F). We then used neonatal CMs from a

*Gja1*$^{M213L/M213L}$ mouse line that was recently generated by mutating the internal AUG (Methionine) at residue 213 of *Gja1* to UUA (Leucine). This M213L mutation removes the internal translation start site, resulting in expression of full length Cx43 protein but not the internally translated GJA1-20k isoform (Xiao et al., 2020). Neonatal CMs from *Gja1*$^{M213L/M213L}$ mice have an increase in their average area of mitochondria (Figure 1C, F), in contrast to the decrease in mitochondrial area of neonatal CMs with GJA1-20k overexpression (Figure 1C, F). Thus, both cultured cells and neonatal mouse cardiomyocytes exhibit an inverse relationship between the presence of GJA1-20k and mitochondrial size.

The homozygous *Gja1*$^{M213L/M213L}$ mice, which lack the expression of GJA1-20k but not full-length Cx43, die from poor gap junction trafficking and arrhythmogenic sudden cardiac death two to four weeks after birth (Xiao et al., 2020). We therefore pre-emptively sacrificed and examined two-week old homozygous *Gja1*$^{M213L/M213L}$ mice, and explored mitochondrial size by electron microscopy (EM). The mitochondria of two-week old cardiomyocytes deficient of GJA1-20k are enlarged (Figure 1D, F). We then delivered exogenous GJA1-20k using adeno-associated virus type 9 (AAV9) to 8 week old adult WT mice (Basheer et al., 2018) and found a decrease in the average mitochondrial area (Figure 1E, F). Taken together, in cell lines, neonatal CM, young mouse hearts, and mature mouse hearts, an increase in GJA1-20k results in smaller mitochondria, whereas a decrease in GJA1-20k results in larger mitochondria.

**Canonical mitochondrial dynamics are not involved**

Mitochondrial dynamics are regulated by well-known mediators including DRP1 for fission (Friedman and Nunnari, 2014), and MFN1 and MFN2 for fusion (Schrepfer and Scorrano, 2016). DRP1 is potentiated by phosphorylation of its Serine 616 (Sabouny and Shutt,

2020). We tested abundance of total DRP1 and phosphorylated DRP1 (DRP1-pS616) in GJA1-20k transfected HEK293 cells and found no significant difference in either the protein levels of total DRP1 or DRP1-pS616 or in the ratio (pS616/total) (Figure 2A, B). The levels of MFN1 and MFN2, and mitochondrial marker protein TOM20, a marker of cellular mitochondrial content, were also unchanged (Figure 2A, B).

To further investigate whether GJA1-20k induced reduction in mitochondrial size is dependent on DRP1, we analyzed mitochondrial morphology after inhibiting DRP1 by treating cells pharmacologically with mitochondrial division inhibitor 1 (Mdivi-1), or by performing siRNA-mediated *DRP1* knock-down (Figure 2—figure supplement 1A), all with or without GJA1-20k transfection. With either method of DRP1 inhibition, the average area of individual mitochondria increased, consistent with inhibiting canonical fission (Figure 2C–F). However, GJA1-20k acts epistatically to DRP1 loss and prevents DRP1-mediated mitochondrial enlargement (Figure 2C–F; Figure 2—figure supplement 1B, C), indicating GJA1-20k can act at or downstream of DRP1 activation.

**GJA1-20k interacts with actin to induce fission**

The actin cytoskeleton and its dynamics have been implicated as fundamental mediators of mitochondrial fission (Korobova et al., 2013, Hatch et al., 2014, Ji et al., 2015, Moore et al., 2016). GJA1-20k has been previously identified to cluster with and stabilize the actin network both in vitro and in vivo (Basheer et al., 2017). We imaged actin in GJA1-20k transfected HEK293 cells and noted that, in the presence of GJA1-20k, actin assembles around mitochondria, forming filamentous rings surrounding the outer membrane (Figure 3A). We used biochemical methods to confirm that GJA1-20k induces association of actin and mitochondria.

Cytosolic and mitochondrial pools of proteins were separated and actin protein levels were measured in each fraction. As seen in Figure 3B, C, the large increase in mitochondrial associated actin occurs in the presence of GJA1-20k. Together these data provide both imaging and biochemical evidence that GJA1-20k recruits the actin cytoskeleton to the mitochondrial membrane.

The actin rings of Figure 3A are filamentous, indicating formation or stabilization of actin polymers. We asked how GJA1-20k alone, which localizes to the mitochondrial outer membrane (Basheer et al., 2018), can recruit and polymerize actin around mitochondria (Figure 3A). Using a reductionist cell-free assay of actin polymerization, we found that GJA1-20k does not directly promote actin polymerization (Figure 3D), and the polymerization kinetics is even slightly slowed down in the presence of GJA1-20K. However, GJA1-20k causes a leftward shift in the polymerization-depolymerization equilibrium (Blanchoin et al., 2014) by directly inhibiting actin depolymerization (Figure 3E). The effect of substantial GJA1-20k, by inhibiting depolymerization, is to cause a net increase in polymerization. Because GJA1-20k enriches at outer mitochondrial membrane (Fu et al., 2017, Basheer et al., 2018), the GJA1-20k induced polymerization will occur at and around the mitochondrial membrane. Interestingly, GJA1-20k results in net actin polymerization even in the presence of Latrunculin A (LatA), a known potent inhibitor of actin polymerization (Fujiwara et al., 2018) (Figure 3E). In cells, it has been reported that LatA increases individual mitochondrial area, consistent with an inhibition of actin-dependent mitochondrial fission (Figure 3F, G)(Korobova et al., 2013, Li et al., 2018, Moore et al., 2016). However, the presence of GJA1-20k counteracts the LatA effect, preserving acting polymerization and preventing an overall increase in mitochondrial size (Figure 3F, G).

Use of fluorescently labelled actin, GJA1-20k, and mitochondria permit real time imaging of mitochondrial fission events at actin assembly sites. As seen in Video 1 and 2; and Figure 4A, C, GJA1-20k recruits actin to mitochondria, which often results in fission. In Video 1 and 2, the actin network can be seen to develop around mitochondria and, coinciding with GJA1-20k intensity, forms an increasingly tight band across a mitochondrion which, within one minute, results in mitochondrial fission. The imaging in the bottom row of Figure 4A, C, and in the right column of Video 1 and 2, were obtained by multiplying GJA1-20k signal with actin signal, highlighting the locations at which GJA1-20k and actin are coincident. The respective line-scan profiles in Figure 4B, D indicate that mitochondrial fission occurs at points where the product of GJA1-20k and actin is the highest. Following accumulation of GJA1-20k and actin (red lines) at these points, a drop in mitochondrial signal (blue lines) is apparent when fission occurs. Fission (low point of blue lines) occurs approximately 45 seconds after co-accumulation of GJA1-20k and actin (high point of red lines, Figure 4B, D). Time to fission was computed from the time of peak GJA1-20k and actin intensity product, to the time of mitochondrial signal being reduced to background (Figure 4E–G). Statistically, this time to fission occurred at a median of 45 seconds, with a standard deviation of 11 seconds (Figure 4H). Note, the real time imaging shown in Video 1 and 2,and Figure 4 were performed in the presence of DRP1 inhibitor Mdivi-1. Therefore, the mitochondrial fission induced by cooperation between GJA1-20k and actin can be independent of canonical DRP1-mediated fission.

**GJA1-20k induces protective effects against oxidative stress**

It has been found that AAV9-mediated GJA1-20k overexpression in mouse heart depresses mitochondrial respiration, which has the beneficial effect of limiting myocardial

193 infarction after ischemic-reperfusion (I/R) injury (Basheer et al., 2018). We measured oxygen
194 consumption rate (OCR) using a Seahorse mitochondrial stress test in GJA1-20k transfected
195 HEK293 cells and found a decrease in maximal respiration (Figure 5A, B), consistent with
196 previous results (Basheer et al., 2018). In contrast, maximal respiration is significantly increased
197 in neonatal CMs derived from GJA1-20k deficient *Gja1*$^{M213L/M213L}$ mice (Figure 5C, D).
198 Given that GJA1-20k is a stress-responsive protein which can mediate ischemic
199 preconditioning (Basheer et al., 2018), we measured reactive oxygen species (ROS) in HEK293
200 cells under oxidative stress induced by exogenous $H_2O_2$ treatment. In unstressed cells, the
201 presence of GJA1-20k does not affect mitochondrial ROS generation (Figure 5E, F) whereas in
202 the presence of exogenous $H_2O_2$, GJA1-20k prevents an increase in mitochondrial ROS (Figure
203 5E, F). Thus, GJA1-20k, which depresses mitochondrial respiration in unstressed cells (Figure
204 5A, B), does not affect homeostatic ROS generation, yet has the beneficial effect of decreasing
205 toxic ROS generation during stress (Figure 5E, F).
206 To explore whether GJA1-20k is necessary to protect against oxidative injury in heart
207 muscle we subjected Langendorff-perfused adult hearts from heterozygous *Gja1*$^{M213L/WT}$ mice to
208 ischemia-reperfusion (I/R) injury. Since homozygous Gja1$^{M213L/M213L}$ mice die in two to four
209 weeks after birth, we used heterozygous *Gja1*$^{M213L/WT}$ mice to be able to work with adult hearts.
210 At baseline, adult *Gja1*$^{M213L/WT}$ mice have no change in overall phenotype, or cardiac chamber
211 dimensions or cardiac functional characteristics compared to WT mice, as measured by
212 echocardiography (Xiao et al., 2020). We also did not find a significant difference in
213 mitochondrial size under basal conditions (Figure 5—figure supplement 1). However,
214 remarkably, reduced GJA1-20k expression results in an almost complete cardiac infarction after

I/R injury (Figure 5G, H). These data indicate that even partial deletion of GJA1-20k results in a profoundly impaired response to ischemic stress.

## Discussion

In conclusion, we find that the stress-responsive protein GJA1-20k organizes actin around mitochondria, promoting an actin-dependent mitochondrial fission process that also protects against oxidative and ischemic stress (cartoon in Figure 6). This protective fission pathway is distinct from canonical DRP1-mediated fission. In heart muscle, GJA1-20k appears to be critical to limit ischemic damage. Adult mice heterozygous for the internal GJA1-20k start have normal baseline cardiac phenotypes, yet suffer almost complete myocardial infarctions once subjected to I/R injury (Figure 5G, H).

Mitochondrial fusion and fission dynamics are understood to involve several key molecules. MFN1 and MFN2 have important roles in fusion (Schrepfer and Scorrano, 2016), while DRP1 mediates canonical fission (Friedman and Nunnari, 2014). A dynamic equilibrium between fusion and fission is important during development as well as in response to a changing cellular environment. Alteration of the equilibrium point between fusion and fission occurs with disease (Chan, 2006). Additionally, in mouse heart, hypertrophy or dilated cardiomyopathy result from either MFN1 or MFN2 deletion (which causes mitochondrial fragmentation) or DRP1 deletion (which causes hyperfused mitochondria)(Song et al., 2015). The implication is that either a leftward or rightward shift in the fusion-fission equilibrium can negatively affect cardiac function. However, it is becoming increasingly clear that mitochondrial size alone, the easiest readout of mitochondrial dynamics, is insufficient to interpret whether destructive or pro-survival pathways are dominant. The presence of GJA1-20k, which increases with ischemic and

oxidative stress (Basheer et al., 2018, Ul-Hussain et al., 2014), is clearly beneficial in the setting of I/R injury (Figure 5G, H). Yet the presence of GJA1-20k, while inducing mitochondrial fission and smaller mitochondria (Figure 1, 3 and 4), does not either reduce MFN1 or MFN2, or activate DRP1 (Figure 2). The ability of GJA1-20k to recruit actin to induce fission independently of DRP1 is novel. GJA1-20k use of actin to cause fission occurs rapidly, within 45 seconds of peak GJA1-20k and actin coincidence at mitochondrial membrane (Figure 4H). The immediate question is that, given these rapid dynamics, how to limit fission in stable cells, especially terminally differentiated cells such as adult cardiomyocytes. We have not yet evaluated whether secondary regulators or post-translational modification of either primary actin or GJA1-20k affects GJA1-20k mediated mitochondrial dynamics. One simple form of regulation is in the abundance of GJA1-20k. The paucity of GJA1-20k at baseline, and its large and rapid increase during the onset of ischemic stress (Basheer et al., 2018), support the role of GJA1-20k as a stress responsive process which affords acute protection during ischemic injury.

While smaller mitochondrial size has been traditionally associated with mitochondrial fragmentation and poor cellular health (Wai and Langer, 2016), it is now understood that there is a more complex relationship between mitochondrial size and mitochondrial function (Sprenger and Langer, 2019). Smaller mitochondria can signal not only disease but also tissue protection and adaptation. DRP1-induced fission and smaller mitochondria are associated with excess ROS production, apoptosis, and organ injury (Hu et al., 2017, Wang et al., 2017), whereas DRP1-independent mitochondrial fission has been observed in cells undergoing protective mitophagy (Stavru et al., 2013, Yamashita et al., 2016, Coronado et al., 2018). It appears that GJA1-20k mediated fission is highly beneficial, and part of a pro-survival cellular response to stress. Our results suggest that mitochondrial morphology (i.e. the overall balance of fusion and fission) in

stressed cells should be considered in the context of the presence of specific proteins. For instance, pathological fission in the presence of activation of DRP1 might indicate mitophagy (Burman et al., 2017, Wang et al., 2017, Ikeda et al., 2015), whereas an increase in GJA1-20k implies a stress-induced reduction of ROS generation and beneficial depression of metabolism. Both DRP1 activation and GJA1-20k generation result in mitochondrial fission, but have different implications for cellular health.

Since its first report 35 years ago, investigators have both tried to understand the mechanisms of preconditioning as well as use putative mediators of precondition to benefit organs undergoing anticipated ischemia. These efforts have included dozens of preclinical and proof-of-concept studies, yet without success (Heusch and Gersh, 2020). Mediators such as cyclophilin D (Cung et al., 2015), cardiolipin (Gibson et al., 2016), mitochondrial permeability transition pore (MPTP)(Atar et al., 2015, Schaller et al., 2010), Cx43 (Schulz et al., 2015), ATP-dependent $K^+$ channels (Heinzel et al., 2005, Garlid et al., 2009) , STAT3 (Heusch et al., 2011), GSK3-beta (Juhaszova et al., 2004), and opioid receptors (Dragasis et al., 2013) have been implicated in preconditioning protection (Heusch and Gersh, 2017), but replicating their involvement in clinical studies has, to present, failed to be successful. More recently, the phenomenon of remote preconditioning has been explored as a therapeutic solution, but clinical application of this approach has also yet to be successful (Heusch and Gersh, 2020). It is possible that the reason a central mediator of preconditioning has not been determined is that it has not been available for study. GJA1-20k was first reported to occur endogenously in 2013 (Smyth and Shaw, 2013) and its association with mitochondria and potential beneficial effects for survival of I/R was only reported in the last three years (Fu et al., 2017, Basheer et al., 2018, Fu et al., 2020, Ren et al., 2020, Wang et al., 2019). As a smaller isoform of Cx43 that contains the epitope of

most anti-Cx43 antibodies, and is localized to mitochondria (Fu et al., 2017), GJA1-20k could be central to the studies that implicated Cx43 as a mediator of preconditioning. As a stress responsive protein (Basheer et al., 2018, Ul-Hussain et al., 2014), endogenous GJA1-20k is induced by short bouts of ischemia prior to a longer ischemic period (Basheer et al., 2018). Because GJA1-20k-induced fission is associated with less ROS production with oxidative stress (Figure 5E, F), the generation of GJA1-20k and subsequent decreased ROS production could explain the major benefit of pre-conditioning. Less ROS production could limit the amount myocardial infarction with I/R injury (Figure 5G, H). Stunned myocardium is a clinical term for quiescent yet viable myocardium post-ischemic injury. The phenomenon of stunned myocardium is common in patients with I/R injury such as experiencing an occluded coronary artery that is revascularized, but the mechanism of stunning is not well elucidated. It is possible that stunned myocardium has elevations of GJA1-20k after the ischemic injury. Of note, stunned myocardium is metabolically quiescent and also exhibits smaller mitochondria (Borgers, 2002, Borgers et al., 1993), further supporting the possibility that GJA1-20k is involved in the stunned response to ischemia as a mechanism of preventing myocardial death. Endogenous induction of GJA1-20k may also explain other instances when smaller mitochondrial size correlates with a beneficial effect (Coronado et al., 2018). Recent studies have identified that exogenous GJA1-20k can protect neurons subjected to traumatic brain injury (Ren et al., 2020), hearts from ischemia (Basheer et al., 2018) and angiotensin induced hypertrophy (Fu et al., 2020). Furthermore, by mimicking the protection afforded by ischemic preconditioning, exogenous GJA1-20k is a promising therapeutic to protect hearts, brains and other organs against expected ischemic damage.

In summary, we identify that upregulation of the stress-responsive internally translated peptide, GJA1-20k, may be a critical mediators of ischemic-preconditioning protection. GJA1-20k induces fission by recruiting actin to mitochondria, inducing a fission that decreases ROS generation and protects organs such as the heart. Use of exogenous GJA1-20k as a therapeutic can potentially realize the long sought yet still elusive clinical need of preventing organs from undergoing damage during anticipated ischemia.

## Materials and Methods

### Animals

All mice were maintained under sterile barrier conditions. For the exogenous gene delivery, we used C57BL6 male mice under same conditions at the age of 8 weeks to start the study procedure according to previous study (Basheer et al., 2018, Basheer et al., 2017). We injected 100 µl of 3 $\times 10^{11}$ vector genomes per mL of Adeno-associated virus type 9 (AAV9) vectors containing GFP-tagged glutathione S-transferase (GST-GFP) or GJA1-20k (GJA1-20k-GFP) driven by the cytomegalovirus (CMV) promoter through retro-orbital injection. Eight weeks post-injection, the heart dissection was performed under anesthesia by isoflurane. Heparin (100 IU, i.p.) was injected 20 – 30 minutes before dissection. We perfused the heart with cold HEPES buffer to wash out the blood and immediately freeze and proceed DNA extraction. The details of $Gja1^{M213L/M213L}$ mouse generation has been described previously (Xiao et al., 2020). We isolated neonatal cardiomyocyte (postnataTl 2 – 3 days) from $Gja1^{M213L/M213L}$ and Wildtype (WT) mice using Pierce™ Primary Cardiomyocyte Isolation Kit (Thermo Fisher Scientific, Walthman, MA) following manufacturer protocol. The neonatal cardiomyocyte was seeded into gelatin/fibronectin coated 35 mm glass-bottomed dish and subjected to imaging as described below. Adenovirus encoding GJA1-20k-V5 (GFP-V5 as a control; 4 plaque-forming unit/cell)

was transduced as previously described (Basheer et al., 2017) followed by live cell imaging. The average area of individual mitochondria in GFP-V5 control myocyte was unchanged compared to WT non-transduced cardiomyocytes (Figure 1—figure supplement 1D, E). We also dissected the heart tissue at the age of two weeks from Gja1$^{M213L/M213L}$ and WT mice under anesthesia described above for the following experiments. All animal care and study protocols were approved by University of Utah Institutional Animal Care and Use Committee.

**Electron microscope imaging**

The mouse hearts were prepared as described previously (Basheer et al., 2018). Briefly, the adult mouse hearts were fixed by perfusing with 2 % glutaraldehyde and 2 % paraformaldehyde in PBS for 10 minutes followed by post-fixed with 1 % osmium tetroxide and incubated in 3 % uranyl acetate. The small hearts from young mouse (two weeks old) dissected into 1 mm pieces were immediately fixed with 2.5% glutaraledehyde, 1% paraformaldehyde, 0.1 M Cacodylate buffer, pH 7.4, 6 mM $CaCl_2$, 4.8% Sucrose, at 4 °C. Following overnaight fixation, the specimens were rinsed 2 times in buffer and were postfixed in 2 % Osmium tetroxide for one hour at room temperature. The specimens were rinsed in $dH_2O$ and pre-stained with uranyl acetate for one hour ate room temperature. Then the samples were dehydrated in graded ethanol series and 3 times in pure acetone then infiltrated and embedded in epoxy resin, Embed 812 (cat # 14121, Electron Microscopy Sciences, Hatfield, PA). The blocks were cut at 70 nm thickness using an ultramicrotome (Leica, Wetzlar, Germany) and poststained with uranyl acetate for 10 minutes, and lead citrate for 5 minutes. Sections were examined at an accelerating voltage of 120 kV in a JEM-1400 plus or JEM1200-EX (JEOL, Tokyo, Japan) transmission electron microscope with CCD Gatan camera. The number and the total area of mitochondria in each image were

354 measured using imageJ and the average area was calculated by dividing the total area by the
355 number. Electron microscope imaging was performed by the core facility at Electron Microscopy
356 Laboratory at University of Utah and at the Electron Imaging Center of The California
357 NanoSystems Institute at University of California, Los Angeles.
358
359 **Cell culture, Plasmid and siRNA transfection, DRP1 inhibition, and Latrunculin A**
360 **treatment**
361 HEK293 cells were cultured with DMEM containing 10 % fetal bovine serum (FBS), non-
362 essential amino acids, sodium pyruvate (Thermo Fisher Scientific), and Mycozap-CL (Lonza) in
363 37 °C, 5 % $CO_2$ incubator. For imaging analysis, we coated 35 mm glass-bottomed dish with 0.1
364 % gelatin (Sigma-Aldrich, St. Louis, MO) and human fibronectin (20 μg/ml, Corning)
365 incubating 37 °C for 2 hours or 4 °C overnight before cell seeding. We seeded the cells (2.0 ×
366 $10^5$ cells/dish) into the coated dishes and harvested in the incubator. Next day, we transfected
367 GST- or GJA1-20k-GFP (0.5 μg/dish) with or without LifeAct-mCherry (1.0 μg/dish) plasmids
368 as described previously (Fu et al., 2017), using FuGene® HD (Promega, Madison, WI) following
369 manufacturer protocol. The constructs are driven by CMV promoter and internal methionine in
370 GJA-20k was mutated to leucine to express a single isoform as described previously (Smyth and
371 Shaw, 2013). After overnight transfection, the cells were subjected to imaging or protein
372 extraction. To obtain enough proteins from 100 mm culture dish, we multiplied the plasmid
373 concentration based on bottom surface area of 35 mm dish (approximately 0.05 μg/$cm^2$). To
374 knock-down Gja1 or DRP1, we used Gja1 siRNA (Thermo Fisher Scientific, ID HSS178257),
375 DRP1 siRNA (Thermo Fisher Scientific, ID 19561), and Stealth RNAiTM (Thermo Fisher
376 Scientific) as negative control. We transfected 25 pmol of siRNA by LipofectamineTM

RNAiMAX (Thermo Fisher Scientific) following manufacturer protocol. After overnight incubation, GST- or GJA1-20k-GFP plasmid was transfected as described above and the samples were subjected to subsequent experiments. To confirm the knock-down, we used 6-well culture plate and proceed knock-down exactly same way and same time followed by protein extraction described below. For pharmacological DRP1 inhibition, a mitochondrial division inhibitor 1 (Mdivi-1, 50 μM) or the equal amount of Dimethyl sulfoxide (DMSO) diluted in culture medium was added to the cells at the same time as the plasmid transfection. After overnight incubation, the samples were subjected to imaging. To disrupt the actin polymerization, the cells after the transfection were incubated for 1 hour with Latrunculin A (LatA; 100 nM) or the equal amount of DMSO diluted in culture medium. After the incubation, the samples were subjected to imaging.

**Confocal live and fixed cell imaging**

We followed the protocol described previously (Fu et al., 2017). The imaging was performed using a Nikon Eclipse Ti imaging system with a ×100/1.49 Apo TIRF objective, a spinning disk confocal unit (Yokogawa, Tokyo, Japan) with 486, 561, and 647 nm diode-pumped solid state lasers, and an ORCA-Flash 4.0 Hamamatsu camera, controlled by NIS Elements software. For live cell imaging, the cells were imaged in culture medium using DMEM without Phenol Red (Thermo Fisher Scientific) for snapshot or time-lapse imaging. The imaging chamber was maintained 37 °C and 5 % $CO_2$. Mitochondria were labeled by incubating 37 °C for 20 minutes with Mitotracker (200 nM, Thermo Fisher Scientific) before imaging. For fixed cell imaging, the cells were fixed by 4 % paraformaldehyde for 30 minutes at room temperature. After fixation, the samples were permeabilized in 0.1 % TritonX-100 in PBS for 10 minutes, washed with PBS

2 × 5 minutes, and blocked in 5 % normal goat serum (NGS) in PBS for 2 hours at room temperature. The following primary antibodies were diluted in 1 % NGS in PBS and incubated in dark moisture chamber at 4 °C overnight; anti-GFP (1:2000, Abcam), anti-TOM20 (1:1000, Abcam), ant-DRP1 (1:250, Abcam). Next day, the samples were washed with PBS 3 × 10 minutes and incubated with host-matched immunoglobin cross-adsorbed secondary antibodies conjugated with Alexa Fluor 488, 555, 647 (1:500, Invitorgen, Carlsbad, CA) in 1% NGS in PBS for 1 hour at room temperature. After washing with PBS 3 × 10 minutes, the samples were mounted with ProLongTM Gold antifade regent with DAPI (Thermo Fisher Scientific). For image analysis, we used ImageJ with the mito-morphology plugin (Dagda et al., 2009) for mitochondrial morphology analysis.

**Western blot analysis**

We performed Western blot as previously described (Basheer et al., 2018). We harvested the cells in 100 mm culture dish or 6-well plate for knock-down experiment transfected plasmid as described above. The cells were lysed by RIPA buffer (containing 50 mM Tris, 150 mM NaCl, 1 mM EDTA, 1 % TritonX-100, 1 % Sodium Deoxycholate, 1 mM NaF, 0.2 mM $Na_3VO_4$, and Halt Proteinase and Phosphatase Inhibitor Cocktail (Thermo Fisher Scientific)) to extract total protein. The lysate was sonicated on ice, rotated for 1 hour at 4 °C, and centrifuged 16,000 ×g for 20 minutes at 4 °C. The supernatant was collected as the protein sample. To extract mitochondrial fraction, we used Mitochondria Isolation Kit for Cultured Cells (Thermo Fisher Scientific) following manufacturer protocol. The protein concentration was measured using DC™ Protein Assay (Bio-Rad, Hercules, CA). The protein samples with sample buffer (NuPAGE LDS sample buffer (NP0007) containing 100 mM DTT) were separated using

NuPAGE Bis-Tris gels (4 – 12 %) with 3-(N-morpholino)propanesulfonic acid (MOPS) or 2-(N-morpholino)ethanesulfonic acid (MES) running buffer (Thermo Fisher Scientific) followed by transferring to polyvinylidene difluoride (PVDF) membrane (Pall Corporation, Port Washington, NY). After the transferring, the membrane was fixed by soaking in methanol, air drying, and rewetting in methanol followed by blocking with 5 % non-fat milk or bovine serum albumin (for phosphorylated protein detection) in Tris-NaCl-Tween (TNT) buffer (containing 150 mM NaCl, 50 mM Tris (pH 8.0), and 0.1 % Tween20) for 1 hour at room temperature. We used following primary antibodies diluted in TNT buffer; anti-Cx43 C-terminus (1:2000, Sigma-Aldrich), anti-DRP1 (1:500, Abcam), anti-phospho-DRP1 at S616 (1:1000, Cell Signaling Technology, Danvers, MA), anti-MFN1 (1:1000, Cell Signaling Technology), anti-MFN2 (1:1000, Abcam), anti-TOM20 (1:500, Santa Cruz, Dallas, TX), anti-Tubulin (1:2000, Abcam, Cambridge, United Kingdom), anti-GFP (1:10000, Abcam), anti-PGC-1α (1:500, Novus Biologicals, Littleton, CO), anti-mtTFA (1:1000, Abcam), anti-actin (1:2000, Sigma-Aldrich), anti-COX IV (1:1000, Abcam), and anti-MEK1/2 (1:1000, Cell Signaling Technology). After overnight primary antibody incubation at 4 °C, the membrane was washed with TNT buffer 3 × 10 minutes and incubated with host-matched immunoglobin cross-adsorbed secondary antibodies conjugated with Alexa Fluor 488, 555, 647 (1:500, Thermo Fisher Scientific) diluted in TNT buffer for 1 hour at room temperature. The membrane was washed with TNT buffer 3 × 10 minutes, soaked in methanol, and air dried followed by the band detection using Chemidoc MP imaging system (Bio-Rad). The band intensity was quantified using Image Lab software (Bio-Rad).

**Protein Purification**

GJA1-20k without the putative transmembrane region (amino acids 236 - 382 of the full-length human Cx43, NCBI reference NP 000156,1) was fused at the N-terminus with a 6 × His tag and a linker, and at the C-terminus with a linker and 10 Aspartic Acids. The fusion construct was cloned into the pET301/CT-DEST vector via Gateway cloning (Thermo Fisher Scientific). The primers to amplify the sequence are: Forward primer: 5' GGGGACAAGTTTGTACAAAA AAGCAGGCTTCAGGAGGTATACATATGCATCATCATCATCATCACGGTGGTGGCGGT TCAGGCGGAGGTGGCTCTGTTAAGGATCGGGTTAAGGGAAAG 3'. Reverse primer: 5' GGGGACCACTTTGTACAAGAAAGCTGGGTCTTACTAATCGTCATCATCGTCATCATC GTCATCATCACTTCCACCACTTCCACCGATCTCCAGGTCATCAGGCCG 3'. The fusion protein was expressed in the E. coli expression strain LOBSTR (Andersen et al., 2013) (Kerafast, Boston, MA) transformed with pTf16, which encodes the chaperone protein tag (TaKaRa Bio, Shiga, Japan), following the manufacturer protocol. Protein expression was induced at 37 °C with 1 mM isopropyl-1-thio-β-galactopyranoside. The bacterial pellet containing induced GJA1-20k was lysed in B-PER Bacterial Protein Extraction Reagent (Thermo Fisher Scientific) containing cOmplete ULTRA Protease Inhibitor Tablets (Sigma-Aldrich) and sonicated and centrifuged to separate soluble proteins. The HisPur Cobalt Purification Kit (Thermo Fisher Scientific) was used to purify the protein following the manufacturer protocol with some buffer substitutions. We used a buffer containing 300 mM NaCl, 50 mM $NaH_2PO_4$, 5 mM 2-mercaptoethanol, pH 8.0 for column equilibration and washing (with addition of 10 mM and 20 mM imidazole for sequential washing steps), and we used an elution buffer containing 300 mM NaCl, 50 mM $NaH_2PO_4$, 150 mM Imidazole, pH 8.0, 10 % glycerol. Before use, the purified protein was concentrated and subjected to a buffer exchange into a final buffer containing 50 mM $NaH_2PO_4$, 150 mM NaCl (pH 8.0) with 10 % glycerol.

468

469 **Cell-free pyrene-actin polymerization and depolymerization assay**

470 The pyrene-actin polymerization and depolymerization assays were performed using the Actin
471 Polymerization Biochem Kit (Cytoskeleton, Inc., Denver, CO) following the manufacturer
472 protocol. Briefly, lyophilized pyrene-conjugated skeletal muscle actin was reconstituted and
473 diluted to a concentration of 1 mg/ml in G-Buffer (5 mM Tris-HCl pH 8.0, 0.2 mM $CaCl_2$, 0.2
474 mM ATP) and polymerized with 0.25× Actin Polymerization Buffer (500 mM KCl, 20 mM
475 $MgCl_2$, 50 mM guanidine carbonate, 10 mM ATP) for 1 hour at room temperature. F-actin was
476 incubated with either 15 nM LatA or an equal volume of DMSO, and/or 1 mM GJA1-20k
477 protein purified as described above. For the polymerization assay, actin was incubated with 1
478 mM GJA1-20k protein before polymerization. The changes in fluorescence were measured in
479 microplate reader (FlexStation 3, Molecular Devices, San Jose, CA) at excitation wavelength
480 365 nm and emission wavelength 407 nm. The data was obtained from duplicate or triplicate
481 experimental repeats.

482

483 **Seahorse mitochondrial respiration assay**

484 The mitochondrial oxygen consumption rate (OCR) was measured using Seahorse XF96
485 analyzer (Agilent, Santa Clara, CA) following the manufacturer protocol and previous study
486 (Zhang et al., 2012). Isolated mouse neonatal cardiomyocytes (CM) described above ($8.0 \times 10^4$
487 cells/well) or GST- or GJA1-20k-transfected HEK293 cells ($1.0 \times 10^4$ cells/well) were seeded
488 into Seahorse XF96 plate. Before seeding neonatal CM, the plate was coated by laminin (20
489 μg/ml). After 1 (HEK293) or 2 days (neonatal CM) incubation at 37 °C, OCR was measured in
490 three time points after injection of oligomycin (2 μM for neonatal CM; 1 μM for HEK293),

arbonyl cyanide 4-(trifluoromethoxy)phenylhydrazone (FCCP; 5 μM for neonatal CM; 1.5 μM for HEK293), and rotenone/antimycin A (R/A; 1 μM each for both neonatal CM and HEK293). The data was normalized by protein concentration in each well. The maximum respiration was calculated by subtracting the third measurement point of R/A treatment from that of FCCP treatment.

**Mitochondrial ROS measurement**

The cells were harvested in 35 mm glass-bottomed dish and transfected plasmid as described above. The samples were treated with $H_2O_2$ (600 μM, Sigma-Aldrich) or PBS as control diluted in culture medium for 30 minutes at 37 °C followed by MitoSOX Red Mitochondrial Superoxide Indicator (5 μM, Thermo Fisher Scientific) for 10 minutes at 37 °C. After the incubation, the samples were subjected to live cell imaging. The intensity of MitoSOX was calculated using the formula; Total cell intensity – (Area of the cell × Mean intensity of background).

**Langendorff-perfused mouse heart I/R injury**

Adult (14- to 16-week-old) male WT or $Gja1^{M213L/WT}$ mice were used for I/R study, as previously described (Basheer et al., 2018) with some modifications. Briefly, mice were injected with 100 U (IP) of heparin 20 minutes prior to IP administration of sodium pentobarbital (200 mg/kg) and hearts were removed quickly by a midsternal incision and placed into ice-cold modified pH 7.4 Krebs-Henseleit (K-H) solution. Then, the heart was attached to Langendorff apparatus, and perfused through the aorta at a constant rate 2.5 ml/min with the Krebs-Henseleit (K-H) solution (pH 7.4) gassed with 95% $O_2$/5% $CO_2$ constantly. The K-H solution temperature was maintained at 37 °C by circulating water bath. After 20 minutes equilibration to achieve a steady state, the

hearts were subjected to 30 minutes of ischemia (no-flow ischemia) followed by 60 minutes of reperfusion. During ischemia, the hearts were immersed in warm K-H solution. After reperfusion, the hearts were sliced in 1 mm thickness and immersed in freshly made 1% triphenyl tetrazolium chloride (TTC) solution for 20 minutes at 37 °C followed by fixation with 4% paraformaldehyde for 30 minutes. Scanned image was analyzed using Image J (NIH). The area of the infarcted region of each slice was measured by semiautomatic threshold color setting, and expressed as a percentage of the total slice area. Infarct size was corrected to the weight of each slice as previously described (Basheer et al., 2018).

**Mitochondrial DNA copy number analysis**

Total DNA was extracted using NucleoSpin Tissue (MACHEREY-NAGEL, Düren, Germany) from the mouse hearts or the cells cultured in 6-well plate following manufacturer protocol. The DNA concentration was measured using NanoDrop 2000 (Thermo Fisher Scientific) and 5 ng/µl of DNA was subjected to Real-Time PCR analysis (Bio-Rad) using Mouse Mitochondrial DNA Copy Number Assay kit (Detroit R&D, Detroit, MI) for the samples from the mouse heart or Human Mitochondrial DNA Monitoring Primer Set (TaKaRa Bio) for the cells following manufacturer protocol.

**Statistical analysis**

Graphs were created and analyzed using Prism 6 software (GraphPad). For two groups comparison, unpaired two-tail Mann-Whitney U-test was performed. For among multiple group comparison, Kruskal-Wallis test with Dunn's post-hoc test or two-way ANOVA with

Bonferroni's post-hoc test was performed. p values of less than 0.05 was considered significant. All data points, exact p values, and statistical data are provided in the source data.

**Acknowledgements**

We acknowledge W. Basheer and D. Hernandez for the technical discussion, S. Ryazantsev and L. Nikolova for electron microscopy, A. Laxman for Seahorse analysis. J.R. is an Investigator of the Howard Hughes Medical Institute.

**Competing interests**

The authors declare no competing interests.

**References**

Andersen, K. R., Leksa, N. C. & Schwartz, T. U. (2013) Optimized E. coli expression strain LOBSTR eliminates common contaminants from His-tag purification. *Proteins,* 81**,** 1857-61.10.1002/prot.24364

Atar, D., Arheden, H., Berdeaux, A., Bonnet, J. L., Carlsson, M., Clemmensen, P., Cuvier, V., Danchin, N., Dubois-Rande, J. L., Engblom, H., Erlinge, D., Firat, H., Halvorsen, S., Hansen, H. S., Hauke, W., Heiberg, E., Koul, S., Larsen, A. I., Le Corvoisier, P., Nordrehaug, J. E., Paganelli, F., Pruss, R. M., Rousseau, H., Schaller, S., Sonou, G., Tuseth, V., Veys, J., Vicaut, E. & Jensen, S. E. (2015) Effect of intravenous TRO40303 as an adjunct to primary percutaneous coronary intervention for acute ST-elevation myocardial infarction: MITOCARE study results. *Eur Heart J,* 36**,** 112-9.10.1093/eurheartj/ehu331

559 Basheer, W. A., Fu, Y., Shimura, D., Xiao, S., Agvanian, S., Hernandez, D. M., Hitzeman, T. C.,
560 Hong, T. & Shaw, R. M. (2018) Stress response protein GJA1-20k promotes
561 mitochondrial biogenesis, metabolic quiescence, and cardioprotection against
562 ischemia/reperfusion injury. *JCI Insight,* 3.10.1172/jci.insight.121900
563 Basheer, W. A., Xiao, S., Epifantseva, I., Fu, Y., Kleber, A. G., Hong, T. & Shaw, R. M. (2017)
564 GJA1-20k Arranges Actin to Guide Cx43 Delivery to Cardiac Intercalated Discs. *Circ*
565 *Res,* 121**,** 1069-1080.10.1161/CIRCRESAHA.117.311955
566 Blanchoin, L., Boujemaa-Paterski, R., Sykes, C. & Plastino, J. (2014) Actin dynamics,
567 architecture, and mechanics in cell motility. *Physiol Rev,* 94**,** 235-
568 63.10.1152/physrev.00018.2013
569 Borgers, M. (2002) Hibernating myocardium: Programmed cell survival or programmed cell
570 death? *Exp Clin Cardiol,* 7**,** 69-72
571 Borgers, M., Thone, F., Wouters, L., Ausma, J., Shivalkar, B. & Flameng, W. (1993) Structural
572 Correlates of Regional Myocardial Dysfunction in Patients with Critical Coronary-Artery
573 Stenosis - Chronic Hibernation. *Cardiovascular Pathology,* 2**,** 237-245.Doi
574 10.1016/1054-8807(93)90030-6
575 Burman, J. L., Pickles, S., Wang, C., Sekine, S., Vargas, J. N. S., Zhang, Z., Youle, A. M.,
576 Nezich, C. L., Wu, X., Hammer, J. A. & Youle, R. J. (2017) Mitochondrial fission
577 facilitates the selective mitophagy of protein aggregates. *J Cell Biol,* 216**,** 3231-
578 3247.10.1083/jcb.201612106
579 Chan, D. C. (2006) Mitochondria: dynamic organelles in disease, aging, and development. *Cell,*
580 125**,** 1241-52.10.1016/j.cell.2006.06.010

581 Coronado, M., Fajardo, G., Nguyen, K., Zhao, M., Kooiker, K., Jung, G., Hu, D. Q., Reddy, S.,
582 Sandoval, E., Stotland, A., Gottlieb, R. A. & Bernstein, D. (2018) Physiological
583 Mitochondrial Fragmentation Is a Normal Cardiac Adaptation to Increased Energy
584 Demand. *Circ Res,* 122**,** 282-295.10.1161/CIRCRESAHA.117.310725
585 Cung, T. T., Morel, O., Cayla, G., Rioufol, G., Garcia-Dorado, D., Angoulvant, D., Bonnefoy-
586 Cudraz, E., Guerin, P., Elbaz, M., Delarche, N., Coste, P., Vanzetto, G., Metge, M.,
587 Aupetit, J. F., Jouve, B., Motreff, P., Tron, C., Labeque, J. N., Steg, P. G., Cottin, Y.,
588 Range, G., Clerc, J., Claeys, M. J., Coussement, P., Prunier, F., Moulin, F., Roth, O.,
589 Belle, L., Dubois, P., Barragan, P., Gilard, M., Piot, C., Colin, P., De Poli, F., Morice, M.
590 C., Ider, O., Dubois-Rande, J. L., Unterseeh, T., Le Breton, H., Beard, T., Blanchard, D.,
591 Grollier, G., Malquarti, V., Staat, P., Sudre, A., Elmer, E., Hansson, M. J., Bergerot, C.,
592 Boussaha, I., Jossan, C., Derumeaux, G., Mewton, N. & Ovize, M. (2015) Cyclosporine
593 before PCI in Patients with Acute Myocardial Infarction. *N Engl J Med,* 373**,** 1021-
594 31.10.1056/NEJMoa1505489
595 Dagda, R. K., Cherra, S. J., 3rd, Kulich, S. M., Tandon, A., Park, D. & Chu, C. T. (2009) Loss of
596 PINK1 function promotes mitophagy through effects on oxidative stress and
597 mitochondrial fission. *J Biol Chem,* 284**,** 13843-55.10.1074/jbc.M808515200
598 Dragasis, S., Bassiakou, E., Iacovidou, N., Papadimitriou, L., Andreas Steen, P., Gulati, A. &
599 Xanthos, T. (2013) The role of opioid receptor agonists in ischemic preconditioning. *Eur*
600 *J Pharmacol,* 720**,** 401-8.10.1016/j.ejphar.2013.10.001
601 Friedman, J. R. & Nunnari, J. (2014) Mitochondrial form and function. *Nature,* 505**,** 335-
602 43.10.1038/nature12985

603 Fu, Y., Zhang, S. S., Xiao, S., Basheer, W. A., Baum, R., Epifantseva, I., Hong, T. & Shaw, R.
604 M. (2017) Cx43 Isoform GJA1-20k Promotes Microtubule Dependent Mitochondrial
605 Transport. *Front Physiol,* 8**,** 905.10.3389/fphys.2017.00905
606 Fu, Y. L., Tao, L., Peng, F. H., Zheng, N. Z., Lin, Q., Cai, S. Y. & Wang, Q. (2020) GJA1-20k
607 attenuates Ang II-induced pathological cardiac hypertrophy by regulating gap junction
608 formation and mitochondrial function. *Acta Pharmacol Sin*.10.1038/s41401-020-0459-6
609 Fujiwara, I., Zweifel, M. E., Courtemanche, N. & Pollard, T. D. (2018) Latrunculin A
610 Accelerates Actin Filament Depolymerization in Addition to Sequestering Actin
611 Monomers. *Curr Biol,* 28**,** 3183-3192 e2.10.1016/j.cub.2018.07.082
612 Garcia-Dorado, D., Rodriguez-Sinovas, A., Ruiz-Meana, M., Inserte, J., Agullo, L. &
613 Cabestrero, A. (2006) The end-effectors of preconditioning protection against myocardial
614 cell death secondary to ischemia-reperfusion. *Cardiovasc Res,* 70**,** 274-
615 85.10.1016/j.cardiores.2006.02.011
616 Garlid, K. D., Costa, A. D., Quinlan, C. L., Pierre, S. V. & Dos Santos, P. (2009)
617 Cardioprotective signaling to mitochondria. *J Mol Cell Cardiol,* 46**,** 858-
618 66.10.1016/j.yjmcc.2008.11.019
619 Gibson, C. M., Giugliano, R. P., Kloner, R. A., Bode, C., Tendera, M., Janosi, A., Merkely, B.,
620 Godlewski, J., Halaby, R., Korjian, S., Daaboul, Y., Chakrabarti, A. K., Spielman, K.,
621 Neal, B. J. & Weaver, W. D. (2016) EMBRACE STEMI study: a Phase 2a trial to
622 evaluate the safety, tolerability, and efficacy of intravenous MTP-131 on reperfusion
623 injury in patients undergoing primary percutaneous coronary intervention. *Eur Heart J,*
624 37**,** 1296-303.10.1093/eurheartj/ehv597

625 Hatch, A. L., Gurel, P. S. & Higgs, H. N. (2014) Novel roles for actin in mitochondrial fission. *J*
626 *Cell Sci,* 127**,** 4549-60.10.1242/jcs.153791
627 Heinzel, F. R., Luo, Y., Li, X., Boengler, K., Buechert, A., Garcia-Dorado, D., Di Lisa, F.,
628 Schulz, R. & Heusch, G. (2005) Impairment of diazoxide-induced formation of reactive
629 oxygen species and loss of cardioprotection in connexin 43 deficient mice. *Circ Res,* 97**,**
630 583-6.10.1161/01.RES.0000181171.65293.65
631 Heusch, G. & Gersh, B. J. (2017) The pathophysiology of acute myocardial infarction and
632 strategies of protection beyond reperfusion: a continual challenge. *Eur Heart J,* 38**,** 774-
633 784.10.1093/eurheartj/ehw224
634 Heusch, G. & Gersh, B. J. (2020) Is Cardioprotection Salvageable? *Circulation,* 141**,** 415-
635 417.10.1161/CIRCULATIONAHA.119.044176
636 Heusch, G., Musiolik, J., Gedik, N. & Skyschally, A. (2011) Mitochondrial STAT3 activation
637 and cardioprotection by ischemic postconditioning in pigs with regional myocardial
638 ischemia/reperfusion. *Circ Res,* 109**,** 1302-8.10.1161/CIRCRESAHA.111.255604
639 Hu, C., Huang, Y. & Li, L. (2017) Drp1-Dependent Mitochondrial Fission Plays Critical Roles
640 in Physiological and Pathological Progresses in Mammals. *Int J Mol Sci,*
641 18.10.3390/ijms18010144
642 Ikeda, Y., Shirakabe, A., Maejima, Y., Zhai, P., Sciarretta, S., Toli, J., Nomura, M., Mihara, K.,
643 Egashira, K., Ohishi, M., Abdellatif, M. & Sadoshima, J. (2015) Endogenous Drp1
644 mediates mitochondrial autophagy and protects the heart against energy stress. *Circ Res,*
645 116**,** 264-78.10.1161/CIRCRESAHA.116.303356

646 Ji, W. K., Hatch, A. L., Merrill, R. A., Strack, S. & Higgs, H. N. (2015) Actin filaments target
647 the oligomeric maturation of the dynamin GTPase Drp1 to mitochondrial fission sites.
648 *Elife,* 4**,** e11553.10.7554/eLife.11553
649 Juhaszova, M., Zorov, D. B., Kim, S. H., Pepe, S., Fu, Q., Fishbein, K. W., Ziman, B. D., Wang,
650 S., Ytrehus, K., Antos, C. L., Olson, E. N. & Sollott, S. J. (2004) Glycogen synthase
651 kinase-3beta mediates convergence of protection signaling to inhibit the mitochondrial
652 permeability transition pore. *J Clin Invest,* 113**,** 1535-49.10.1172/JCI19906
653 Korobova, F., Ramabhadran, V. & Higgs, H. N. (2013) An actin-dependent step in mitochondrial
654 fission mediated by the ER-associated formin INF2. *Science,* 339**,** 464-
655 7.10.1126/science.1228360
656 Li, G. B., Zhang, H. W., Fu, R. Q., Hu, X. Y., Liu, L., Li, Y. N., Liu, Y. X., Liu, X., Hu, J. J.,
657 Deng, Q., Luo, Q. S., Zhang, R. & Gao, N. (2018) Mitochondrial fission and mitophagy
658 depend on cofilin-mediated actin depolymerization activity at the mitochondrial fission
659 site. *Oncogene,* 37**,** 1485-1502.10.1038/s41388-017-0064-4
660 Moore, A. S., Wong, Y. C., Simpson, C. L. & Holzbaur, E. L. (2016) Dynamic actin cycling
661 through mitochondrial subpopulations locally regulates the fission-fusion balance within
662 mitochondrial networks. *Nat Commun,* 7**,** 12886.10.1038/ncomms12886
663 Murry, C. E., Jennings, R. B. & Reimer, K. A. (1986) Preconditioning with ischemia: a delay of
664 lethal cell injury in ischemic myocardium. *Circulation,* 74**,** 1124-
665 36.10.1161/01.cir.74.5.1124
666 Nishimura, A., Shimauchi, T., Tanaka, T., Shimoda, K., Toyama, T., Kitajima, N., Ishikawa, T.,
667 Shindo, N., Numaga-Tomita, T., Yasuda, S., Sato, Y., Kuwahara, K., Kumagai, Y.,
668 Akaike, T., Ide, T., Ojida, A., Mori, Y. & Nishida, M. (2018) Hypoxia-induced

669 interaction of filamin with Drp1 causes mitochondrial hyperfission-associated myocardial
670 senescence. *Sci Signal,* 11.10.1126/scisignal.aat5185
671 Nunnari, J. & Suomalainen, A. (2012) Mitochondria: in sickness and in health. *Cell,* 148**,** 1145-
672 59.10.1016/j.cell.2012.02.035
673 Picard, M., Shirihai, O. S., Gentil, B. J. & Burelle, Y. (2013) Mitochondrial morphology
674 transitions and functions: implications for retrograde signaling? *Am J Physiol Regul*
675 *Integr Comp Physiol,* 304**,** R393-406.10.1152/ajpregu.00584.2012
676 Ren, D., Zheng, P., Feng, J., Gong, Y., Wang, Y., Duan, J., Zhao, L., Deng, J., Chen, H., Zou, S.,
677 Hong, T. & Chen, W. (2020) Overexpression of Astrocytes-Specific GJA1-20k Enhances
678 the Viability and Recovery of the Neurons in a Rat Model of Traumatic Brain Injury.
679 *ACS Chem Neurosci,* 11**,** 1643-1650.10.1021/acschemneuro.0c00142
680 Rodriguez-Sinovas, A., Ruiz-Meana, M., Denuc, A. & Garcia-Dorado, D. (2018) Mitochondrial
681 Cx43, an important component of cardiac preconditioning. *Biochim Biophys Acta*
682 *Biomembr,* 1860**,** 174-181.10.1016/j.bbamem.2017.06.011
683 Sabouny, R. & Shutt, T. E. (2020) Reciprocal Regulation of Mitochondrial Fission and Fusion.
684 *Trends Biochem Sci,* 45**,** 564-577.10.1016/j.tibs.2020.03.009
685 Salat-Canela, C., Sese, M., Peula, C., Ramon y Cajal, S. & Aasen, T. (2014) Internal translation
686 of the connexin 43 transcript. *Cell Commun Signal,* 12**,** 31.10.1186/1478-811X-12-31
687 Schaller, S., Paradis, S., Ngoh, G. A., Assaly, R., Buisson, B., Drouot, C., Ostuni, M. A.,
688 Lacapere, J. J., Bassissi, F., Bordet, T., Berdeaux, A., Jones, S. P., Morin, D. & Pruss, R.
689 M. (2010) TRO40303, a new cardioprotective compound, inhibits mitochondrial
690 permeability transition. *J Pharmacol Exp Ther,* 333**,** 696-706.10.1124/jpet.110.167486

691 Schrepfer, E. & Scorrano, L. (2016) Mitofusins, from Mitochondria to Metabolism. *Mol Cell,* 61**,**
692 683-694.10.1016/j.molcel.2016.02.022
693 Schulz, R., Gorge, P. M., Gorbe, A., Ferdinandy, P., Lampe, P. D. & Leybaert, L. (2015)
694 Connexin 43 is an emerging therapeutic target in ischemia/reperfusion injury,
695 cardioprotection and neuroprotection. *Pharmacol Ther,* 153**,** 90-
696 106.10.1016/j.pharmthera.2015.06.005
697 Shirakabe, A., Zhai, P., Ikeda, Y., Saito, T., Maejima, Y., Hsu, C. P., Nomura, M., Egashira, K.,
698 Levine, B. & Sadoshima, J. (2016) Drp1-Dependent Mitochondrial Autophagy Plays a
699 Protective Role Against Pressure Overload-Induced Mitochondrial Dysfunction and
700 Heart Failure. *Circulation,* 133**,** 1249-63.10.1161/CIRCULATIONAHA.115.020502
701 Smyth, J. W. & Shaw, R. M. (2013) Autoregulation of connexin43 gap junction formation by
702 internally translated isoforms. *Cell Rep,* 5**,** 611-8.10.1016/j.celrep.2013.10.009
703 Song, M., Mihara, K., Chen, Y., Scorrano, L. & Dorn, G. W., 2nd (2015) Mitochondrial fission
704 and fusion factors reciprocally orchestrate mitophagic culling in mouse hearts and
705 cultured fibroblasts. *Cell Metab,* 21**,** 273-286.10.1016/j.cmet.2014.12.011
706 Sprenger, H. G. & Langer, T. (2019) The Good and the Bad of Mitochondrial Breakups. *Trends*
707 *Cell Biol,* 29**,** 888-900.10.1016/j.tcb.2019.08.003
708 Stavru, F., Palmer, A. E., Wang, C., Youle, R. J. & Cossart, P. (2013) Atypical mitochondrial
709 fission upon bacterial infection. *Proc Natl Acad Sci U S A,* 110**,** 16003-
710 8.10.1073/pnas.1315784110
711 Suen, D. F., Norris, K. L. & Youle, R. J. (2008) Mitochondrial dynamics and apoptosis. *Genes*
712 *Dev,* 22**,** 1577-90.10.1101/gad.1658508

713 Ul-Hussain, M., Olk, S., Schoenebeck, B., Wasielewski, B., Meier, C., Prochnow, N., May, C.,
714 Galozzi, S., Marcus, K., Zoidl, G. & Dermietzel, R. (2014) Internal ribosomal entry site
715 (IRES) activity generates endogenous carboxyl-terminal domains of Cx43 and is
716 responsive to hypoxic conditions. *J Biol Chem,* 289**,** 20979-90.10.1074/jbc.M113.540187
717 Wai, T. & Langer, T. (2016) Mitochondrial Dynamics and Metabolic Regulation. *Trends*
718 *Endocrinol Metab,* 27**,** 105-117.10.1016/j.tem.2015.12.001
719 Wang, M., Smith, K., Yu, Q., Miller, C., Singh, K. & Sen, C. K. (2019) Mitochondrial connexin
720 43 in sex-dependent myocardial responses and estrogen-mediated cardiac protection
721 following acute ischemia/reperfusion injury. *Basic Res Cardiol,* 115**,** 1.10.1007/s00395-
722 019-0759-5
723 Wang, Y., Subramanian, M., Yurdagul, A., Jr., Barbosa-Lorenzi, V. C., Cai, B., de Juan-Sanz, J.,
724 Ryan, T. A., Nomura, M., Maxfield, F. R. & Tabas, I. (2017) Mitochondrial Fission
725 Promotes the Continued Clearance of Apoptotic Cells by Macrophages. *Cell,* 171**,** 331-
726 345 e22.10.1016/j.cell.2017.08.041
727 Xiao, S., Shimura, D., Baum, R., Hernandez, D. M., Agvanian, S., Nagaoka, Y., Katsumata, M.,
728 Lampe, P. D., Kleber, A. G., Hong, T. & Shaw, R. M. (2020) Auxiliary trafficking
729 subunit GJA1-20k protects Connexin43 from degradation and limits ventricular
730 arrhythmias. *J Clin Invest*.10.1172/JCI134682
731 Yamashita, S. I., Jin, X., Furukawa, K., Hamasaki, M., Nezu, A., Otera, H., Saigusa, T.,
732 Yoshimori, T., Sakai, Y., Mihara, K. & Kanki, T. (2016) Mitochondrial division occurs
733 concurrently with autophagosome formation but independently of Drp1 during
734 mitophagy. *J Cell Biol,* 215**,** 649-665.10.1083/jcb.201605093

735 Youle, R. J. & van der Bliek, A. M. (2012) Mitochondrial fission, fusion, and stress. *Science,*
736 337**,** 1062-5.10.1126/science.1219855
737 Zhang, J., Nuebel, E., Wisidagama, D. R., Setoguchi, K., Hong, J. S., Van Horn, C. M., Imam, S.
738 S., Vergnes, L., Malone, C. S., Koehler, C. M. & Teitell, M. A. (2012) Measuring energy
739 metabolism in cultured cells, including human pluripotent stem cells and differentiated
740 cells. *Nat Protoc,* 7**,** 1068-85.10.1038/nprot.2012.048

741

742

## Figure legends

**Figure 1. GJA1-20k decreases in mitochondrial size.**

(**A**)–(**C**) Representative live cell images of mitochondria in HEK293 (**A**, GST- or GJA1-20k-transfected; **B**, Control and siGja1) and mouse neonatal cardiomyocytes (**C**, WT, GJA1-20k-transducted, and Gja1$^{M213L/M213L}$). The right-most panels are magnified images. (**D**) and (**E**) Representative EM images from young mouse hearts (**D**, WT or Gja1$^{M213L/M213L}$) and adult mouse hearts (**E**, GST- or GJA1-20k-injected). (**F**) Summary of the fold change in the average area of mitochondria. (n = 51 (GST), 67 (GJA1-20k), 52 (Control), or 57 (siGja1) HEK293 cells from five independent experiments; n = 46 (WT), 47 (GJA1-20k), or 48 (Gja1$^{M213L/M213L}$) cells from 4 hearts; n = 84 (WT) or 91 (Gja1$^{M213L/M213L}$) images from 6 hearts; n = 25 (GST), or 28 (GJA1-20k) images from 3 hearts. Graphs were expressed as mean ± SD (HEK293) or ± SEM (mouse). p values were determined by two-tailed Mann-Whitney U-test or Kruskal-Wallis test with Dunn's post-hoc test. **p < 0.01, ***p < 0.001. Scale bars, 10 μm and 5 μm in magnified (**A**–**C**); 2 μm (**D** and **E**). Exact p values and statistical data are provided in the source data.

**Figure 2. DRP1 is not involved in GJA1-20k mediated mitochondrial fission.**

(**A**) and (**B**), Western blot analysis for mitochondrial dynamics related proteins. Transfection was confirmed by GFP bands and the band size difference in GFP is due to the difference in molecular weight between GST and GJA1-20k (**A**). Tubulin was used as internal loading control. n = 5 independent experimental repeats. (**C**) and (**E**) Representative fixed cell images of mitochondria (visualized by Tom20) with or without Mdivi-1 (**C**) or DRP1 siRNA treatment (**E**). (**D**) and (**F**) The fold change in the average area of mitochondria in each treatment. n = 32 (GST, DMSO), 33 (GJA1-20k, DMSO), or 29 (GST or GJA1-20k, Mdivi-1) cells (**D**); n = 34 (GST,

control siRNA), 32 (GJA1-20k, control siRNA), 36 (GST, DRP1 siRNA), or 31 (GJA1-20k, DRP1 siRNA) cells (**F**) from three independent experiments. Graphs were expressed as mean ± SD. p values were determined by two-tailed Mann-Whitney U-test or two-way ANOVA with Bonferroni's post-hoc test. ***p < 0.001; n.s., not significant. Scale bars, 5 μm (**C** and **E**). Exact p values and statistical data are provided in the source data.

**Figure 3. GJA1-20k stabilizes and recruits actin around mitochondria for fission.**

(**A**) Representative live cell images of mitochondria with or without GJA1-20k. Actin was labeled by co-transfection with lifeAct-mCherry. The right-most panels indicate magnified images. (**B**) and (**C**) Western blot analysis in cytosol or mitochondrial fraction. MEK1/2 was used as cytosol marker and Tom20 and COX IV as mitochondrial markers (**B**). Quantification of actin in mitochondrial fraction normalized by Tom20 expression (**C**). n = 4 independent experimental repeats. (**D**) and (**E**) Cell-free actin polymerization (**D**) and depolymerization (**E**) assay. (**F**) Representative fixed cell images of mitochondria (visualized by Tom20) with or without LatA. (**G**) The fold change in the average area of mitochondria with or without LatA treatment. n = 32 (GST, DMSO), 33 (GST, LatA), 28 (GJA1-20k, DMSO), or 32 (GJA1-20k, LatA) cells from three independent experiments. Graphs were expressed as mean ± SD. p values were determined by two-tailed Mann-Whitney U-test or two-way ANOVA with Bonferroni's post-hoc test. *p <0.05, ***p < 0.001; n.s., not significant. Scale bars, 10 μm (**F**), 5 μm (**A** and magnified in **F**) and 2 μm (magnified in **A**). Exact p values and statistical data are provided in the source data.

**Figure 4. Time course of mitochondria dynamics and actin acumulation at the mitochondrial fission site under Mdivi-1 treatment.**

(**A**) and (**C**) Representative mitochondrial dynamics in GJA1-20k-transfected cells by time-lapse live cell imaging under Mdivi-1 treatment. The bottom images (with fire look-up table) indicate the product of GJA1-20k and actin signals. The white lines indicate mitochondrial outlines. Scale bars, 2 μm. (**B**) and (**D**) The intensity of mitochondria and the product of GJA1-20k and actin from (**A**) and (**C**), respectively. The colored areas indicate fission sites along the lines shown in each respective insert. (**E**)–(**G**) The time course of the product of GJA1-20k and actin intensity (**E**), mitochondrial intensity (**F**), or combined relative intensity (**G**) at the fission site from the mitochondrion shown in (**A**). Curves are four parameter logistic (4PL) fits to the data. Time 0 corresponds to the peak product of actin and GJA1-20k intensity. The arrows indicate the time point at which fission is complete. (**H**) Measured time from peak product of actin and GJA1-20k intensity to fission in seconds (bars indicate median and 95% confidence interval). n = 29 events. All data points are provided in the source data.

**Figure 5. Mitochondrial metabolic function is preserved by GJA1-20k.**

(**A**)–(**D**) Real-time change in OCR by Seahorse assay and the maximum respiration in HEK293 cells (**A** and **B**) and mouse neonatal CM (**C** and **D**). 7 (GST) or 8 (GJA1-20k) replicates from HEK293 cells; n = 24 (WT from 4 hearts) or 16 ($Gja1^{M213L/M213L}$ from 3 hearts) replicates. (**E**) Representative live cell images of MitoSOX with or without $H_2O_2$ treatment to GST- or GJA1-20k-transfected HEK293 cells. (**F**) Relative intensity of MitoSOX. n = 39 (GST, PBS), 41 (GST, $H_2O_2$), or 37 (GJA1-20k, PBS or $H_2O_2$) cells from three independent experiments. (**G**) Representative images of TTC stained hearts from WT and $Gja1^{M213L/WT}$ mice after I/R. (**H**)

Quantification of infarct size after I/R. n = 4. Graphs were expressed as mean ± SD (HEK293) or SEM (mouse). p values were determined by two-tailed Mann-Whitney U-test or two-way ANOVA with Bonferroni's post-hoc test. *p < 0.05, ***p < 0.001; n.s., not significant. Scale bars, 10 μm (**E**); 5 mm (**G**). Exact p values and statistical data are provided in the source data.

**Figure 6. Schematic summary.**

GJA1-20k, internally translated from Gja1 mRNA, localizes mitochondria membrane, stabilizes actin cytoskeleton, and recruits actin around mitochondria to both induce mitochondrial fission and achieve oxidative stress resistance.

**Movie 1. GJA1-20k assembles actin to mitochondrial fission sites and causes fission (clip 1).**

The mitochondrial fission in GJA1-20k-transfected HEK293 cells was monitored under Mdivi-1 treatment. GJA1-20k (tagged with GFP, green) and mitochondria (indicated by Mitotracker, blue) were simultaneously imaged (left panel), as were mitochondria and actin (indicated by LifeAct-mCherry, red) (middle panel). The spatial coincidence of GJA1-20k and actin were obtained by multiplying GJA1-20k signal with mitochondrial signal, as indicate with a polychromatic fire lookup table (right panel). Note GJA1-20k then actin surround the mitochondria, assembles at the neck of fission site, resulting in fission. The white arrowhead indicates the fission point. Images for each timepoint were obtained every 3 seconds. There are 26 images for a 78 second clip, played back at 5 frames per second (about 15 times as fast as real time). Still frames are indicated in Figure 4A.

**Movie 2. GJA1-20k assembles actin to mitochondrial fission sites and causes fission (clip 2).** The mitochondrial fission in GJA1-20k-transfected HEK293 cells was monitored under Mdivi-1 treatment. GJA1-20k (tagged with GFP, green) and mitochondria (indicated by Mitotracker, blue) were simultaneously imaged (left panel), as were mitochondria and actin (indicated by LifeAct-mCherry, red) (middle panel). The spatial coincidence of GJA1-20k and actin were obtained by multiplying GJA1-20k signal with mitochondrial signal, as indicate with a polychromatic fire lookup table (right panel). Note GJA1-20k then actin surround the mitochondria, assembles at the neck of fission site, resulting in fission. The white arrowhead indicates the fission point. Images for each timepoint were obtained every 3 seconds. There are 81 images for a 243 second clip, played back at 5 frames per second (about 15 times as fast as real time). Still frames are indicated in Figure 4C.

**Figure Supplements**

**Figure 1—figure supplement 1**

**The confirmation of Gja1 knock-down and the mitochondrial morphology rescued by GJA1-20k.**

(**A**) Western blot analysis for Gja1 knock-down by siRNA. Tubulin was used as internal loading control. n = 3 independent experimental repeats. (**B**) The representative confocal live cell imaging of Gja1 knocked-down HEK293 cells with Cx43-M6L or GJA1-20k transfection. (**C**) The fold change in the average area of individual mitochondria. n = 52 (Control), 57 (siGja1), 60 (siGja1 + M6L), or 64 (siGja1 + GJA1-20k) cells from five independent experiments. The images and the values of Control and siGja1 are also shown in Figure 1. (**D**) The representative live cell imaging of mitochondria in WT mouse neonatal CMs with adenovirus-mediated GFP

induction. The right panel indicates magnified image surrounded by square. (**E**) The fold change in the average area of individual mitochondria between WT (no virus introduction, the image and the value shown in Figure 1) and GFP-V5 introduction. n = 46 (WT) or 35 (GFP) cells from 4 hearts. Graphs were expressed as mean ± SD (**C**) or SEM (**E**). p values were determined by two-tailed Mann-Whitney U-test or Kruskal-Wallis test with Dunn's post-hoc test. *p < 0.05, **p < 0.01, ***p < 0.001; n.s., not significant. Scale bars, 10 μm or 5 μm in magnified image. Exact p values and statistical data are provided in the source data.

**Figure 2—figure supplement 1**

**The confirmation of DRP1 knock-down by siRNA and the mitochondrial morphology rescued by GJA1-20k.**

(**A**) Western blot analysis for DRP1 knock-down by siRNA. n = 3 independent experimental repeats. (**B**) and (**C**) The representative fixed cell images of mitochondria (visualized by Tom20) with or without Mdivi-1 (**B**), or siDRP1 (**C**) treatment. The magnified mitochondria images surrounded by the square are used in Figure 2. Scale bars, 10 μm (**B** and **C**) or 5 μm in magnified image (**C**).

**Figure 5—figure supplement 1**

**The mitochondria size did not change in adult mouse heart between WT and heterozygous Gja1$^{M213L/WT}$.**

(**A**) The representative electron microscope images from adult mouse hearts (WT or Gja1$^{M213L/WT}$). Scale bars, 2 μm. (**B**) The fold change in the average area of individual mitochondria. n = 43 (WT) or 46 (Gja1$^{M213L/WT}$) images from 3 hearts. Graph was expressed as

mean ± SEM. p value was determined by two-tailed Mann-Whitney U-test. n.s., not significant. Exact p values and statistical data are provided in the source data.

**Source Data Legends**

**Figure 1—source data 1**

**All data points of the mitochondrial size and the statistical data for Figure 1F.**

**Figure 2—source data 1**

**All data points of the protein expression and the mitochondrial size and the statistical data for Figure 2.**

**Figure 3—source data 1**

**All data points of the actin assay and the mitochondrial size and the statistical data for Figure 3.**

**Figure 4—source data 1**

**All data points of the intensity for Figure 4.**

**Figure 5—source data 1**

**All data points of the seahorse assay, ROS intensity, and infarct size and the statistical data for Figure 5.**

Figure 1

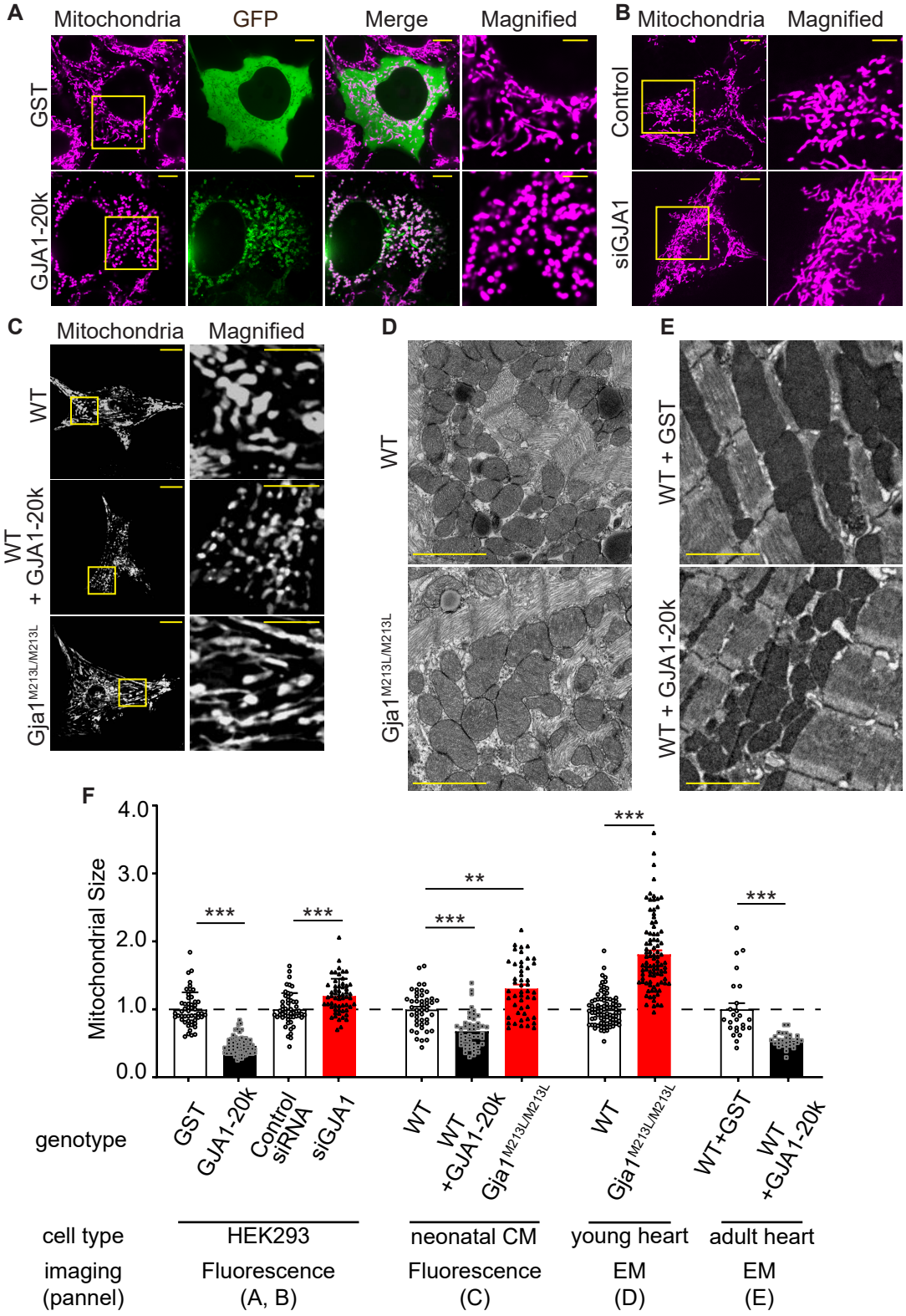


**Figure 1. GJA1-20k decreases in mitochondrial size**

(**A**)–(**C**) Representative live cell images of mitochondria in HEK293 (**A**, GST- or GJA1-20k-transfected; **B**, Control and siGja1) and mouse neonatal cardiomyocytes (**C**, WT, GJA1-20k-transducted, and Gja1$^{M213L/M213L}$). The right-most panels are magnified images. (**D**) and (**E**) Representative EM images from young mouse hearts (**D**, WT or Gja1$^{M213L/M213L}$) and adult mouse hearts (**E**, GST- or GJA1-20k-injected). (**F**) Summary of the fold change in the average area of mitochondria. (n = 51 (GST), 67 (GJA1-20k), 52 (Control), or 57 (siGja1) HEK293 cells from five independent experiments; n = 46 (WT), 47 (GJA1-20k), or 48 (Gja1$^{M213L/M213L}$) cells from 4 hearts; n = 84 (WT) or 91 (Gja1$^{M213L/M213L}$) images from 6 hearts; n = 25 (GST), or 28 (GJA1-20k) images from 3 hearts. Graphs were expressed as mean ± SD (HEK293) or ± SEM (mouse). p values were determined by two-tailed Mann-Whitney U-test or Kruskal-Wallis test with Dunn's post-hoc test. **p < 0.01, ***p < 0.001. Scale bars, 10 μm and 5 μm in magnified (**A**–**C**); 2 μm (**D** and **E**). Exact p values and statistical data are provided in the source data.

Figure 2

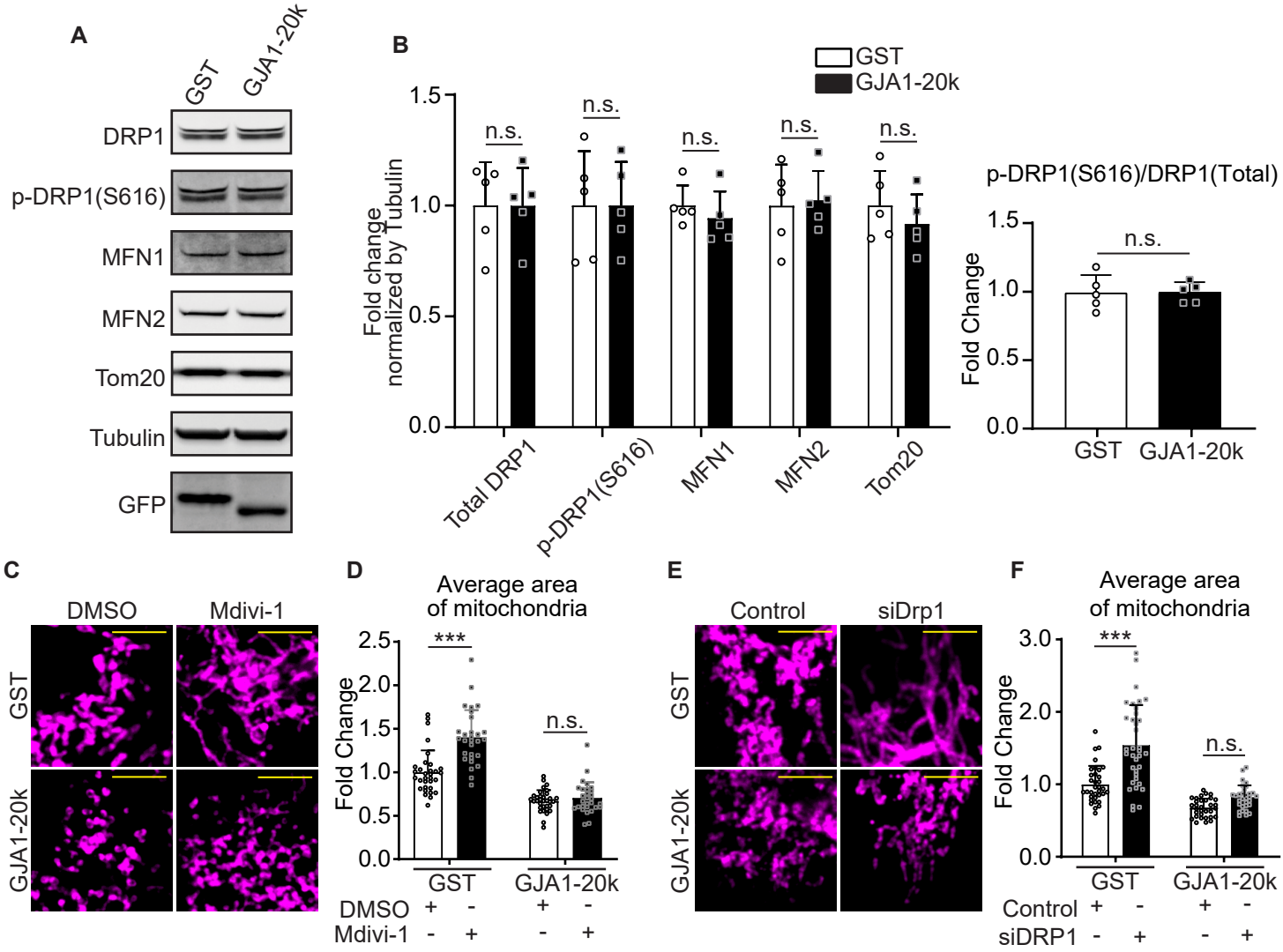


**Figure 2. DRP1 is not involved in GJA1-20k mediated mitochondrial fission**

(**A**) and (**B**), Western blot analysis for mitochondrial dynamics related proteins. Transfection was confirmed by GFP bands and the band size difference in GFP is due to the difference in molecular weight between GST and GJA1-20k (**A**). Tubulin was used as internal loading control. n = 5 independent experimental repeats. (**C**) and (**E**) Representative fixed cell images of mitochondria (visualized by Tom20) with or without Mdivi-1 (**C**) or DRP1 siRNA treatment (**E**). (**D**) and (**F**) The fold change in the average area of mitochondria in each treatment. n = 32 (GST, DMSO), 33 (GJA1-20k, DMSO), or 29 (GST or GJA1-20k, Mdivi-1) cells (**D**); n = 34 (GST, control siRNA), 32 (GJA1-20k, control siRNA), 36 (GST, DRP1 siRNA), or 31 (GJA1-20k, DRP1 siRNA) cells (**F**) from three independent experiments. Graphs were expressed as mean ± SD. p values were determined by two-tailed Mann-Whitney U-test or two-way ANOVA with Bonferroni's post-hoc test. ***$p < 0.001$; n.s., not significant. Scale bars, 5 μm (**C** and **E**). Exact p values and statistical data are provided in the source data.

Figure 3

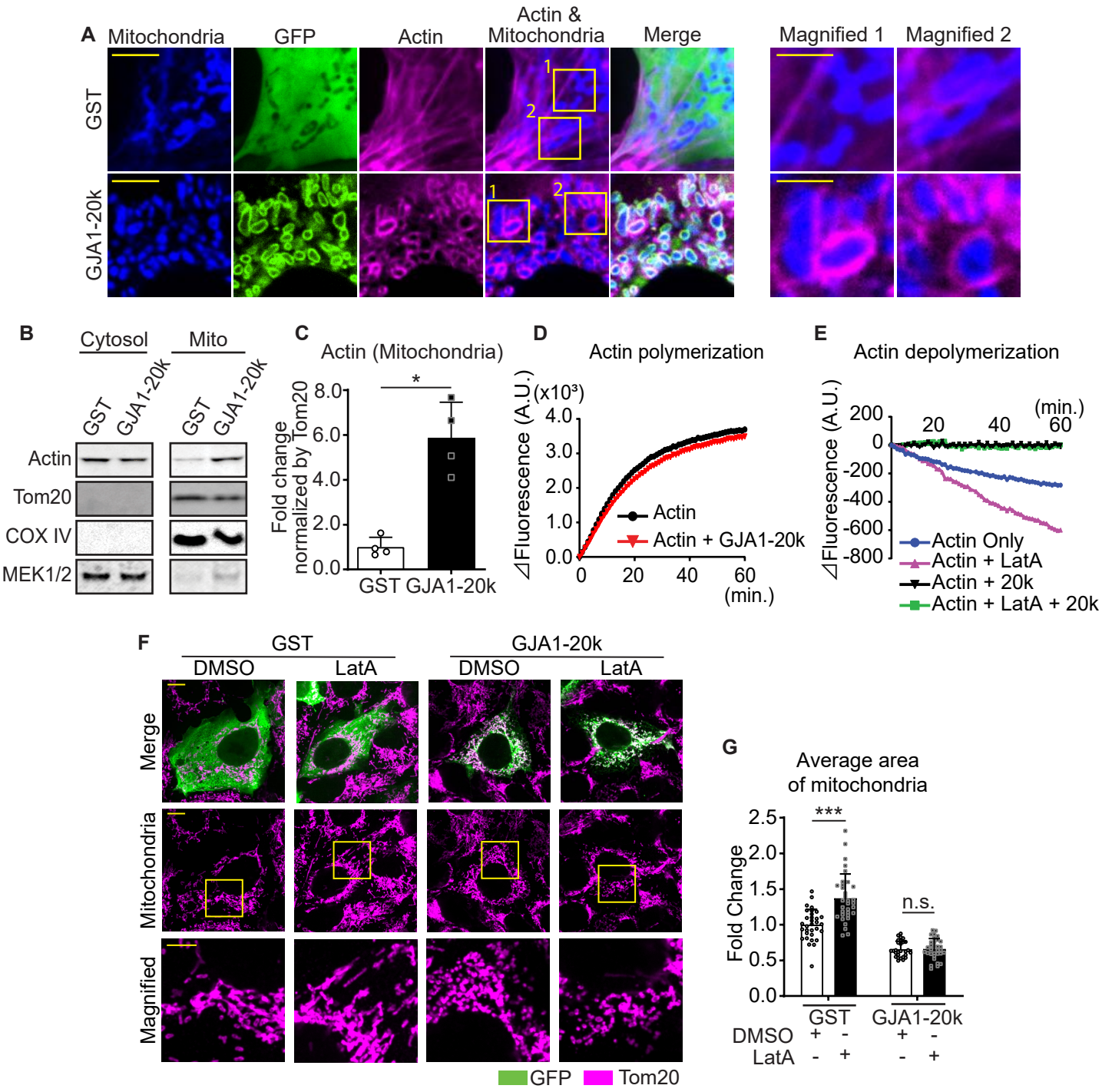


**Figure 3. GJA1-20k stabilizes and recruits actin around mitochondria for fission**

(**A**) Representative live cell images of mitochondria with or without GJA1-20k. Actin was labeled by co-transfection with lifeAct-mCherry. The right-most panels indicate magnified images. (**B**) and (**C**) Western blot analysis in cytosol or mitochondrial fraction. MEK1/2 was used as cytosol marker and Tom20 and COX IV as mitochondrial markers (**B**). Quantification of actin in mitochondrial fraction normalized by Tom20 expression (**C**). n = 4 independent experimental repeats. (**D**) and (**E**) Cell-free actin polymerization (**D**) and depolymerization (**E**) assay. (**F**) Representative fixed cell images of mitochondria (visualized by Tom20) with or without LatA. (**G**) The fold change in the average area of mitochondria with or without LatA treatment. n = 32 (GST, DMSO), 33 (GST, LatA), 28 (GJA1-20k, DMSO), or 32 (GJA1-20k, LatA) cells from three independent experiments. Graphs were expressed as mean ± SD. p values were determined by two-tailed Mann-Whitney U-test or two-way ANOVA with Bonferroni's post-hoc test. *p <0.05, ***p < 0.001; n.s., not significant. Scale bars, 10 μm (**F**), 5 μm (**A** and magnified in **F**) and 2 μm (magnified in **A**). Exact p values and statistical data are provided in the source data.

Figure 4

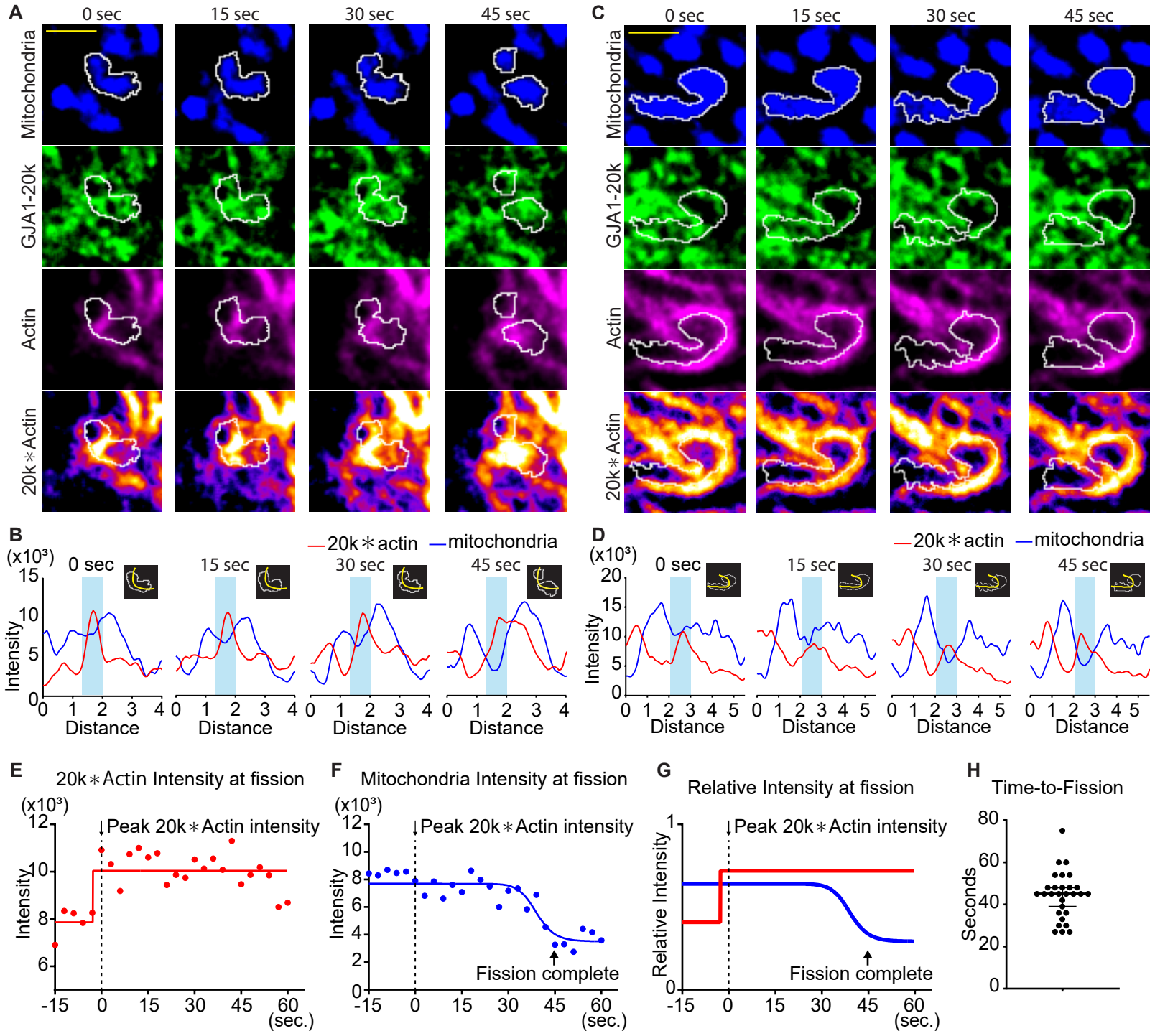


**Figure 4. Time course of mitochondria dynamics and actin acumulation at the mitochondrial fission site under Mdivi-1 treatment**

(**A**) and (**C**) Representative mitochondrial dynamics in GJA1-20k-transfected cells by time-lapse live cell imaging under Mdivi-1 treatment. The bottom images (with fire look-up table) indicate the product of GJA1-20k and actin signals. The white lines indicate mitochondrial outlines. Scale bars, 2 μm. (**B**) and (**D**) The intensity of mitochondria and the product of GJA1-20k and actin from (**A**) and (**C**), respectively. The colored areas indicate fission sites along the lines shown in each respective insert. (**E**)–(**G**) The time course of the product of GJA1-20k and actin intensity (**E**), mitochondrial intensity (**F**), or combined relative intensity (**G**) at the fission site from the mitochondrion shown in (**A**). Curves are four parameter logistic (4PL) fits to the data. Time 0 corresponds to the peak product of actin and GJA1-20k intensity. The arrows indicate the time point at which fission is complete. (**H**) Measured time from peak product of actin and GJA1-20k intensity to fission in seconds (bars indicate median and 95% confidence interval). n = 29 events. All data points are provided in the source data.

Figure 5

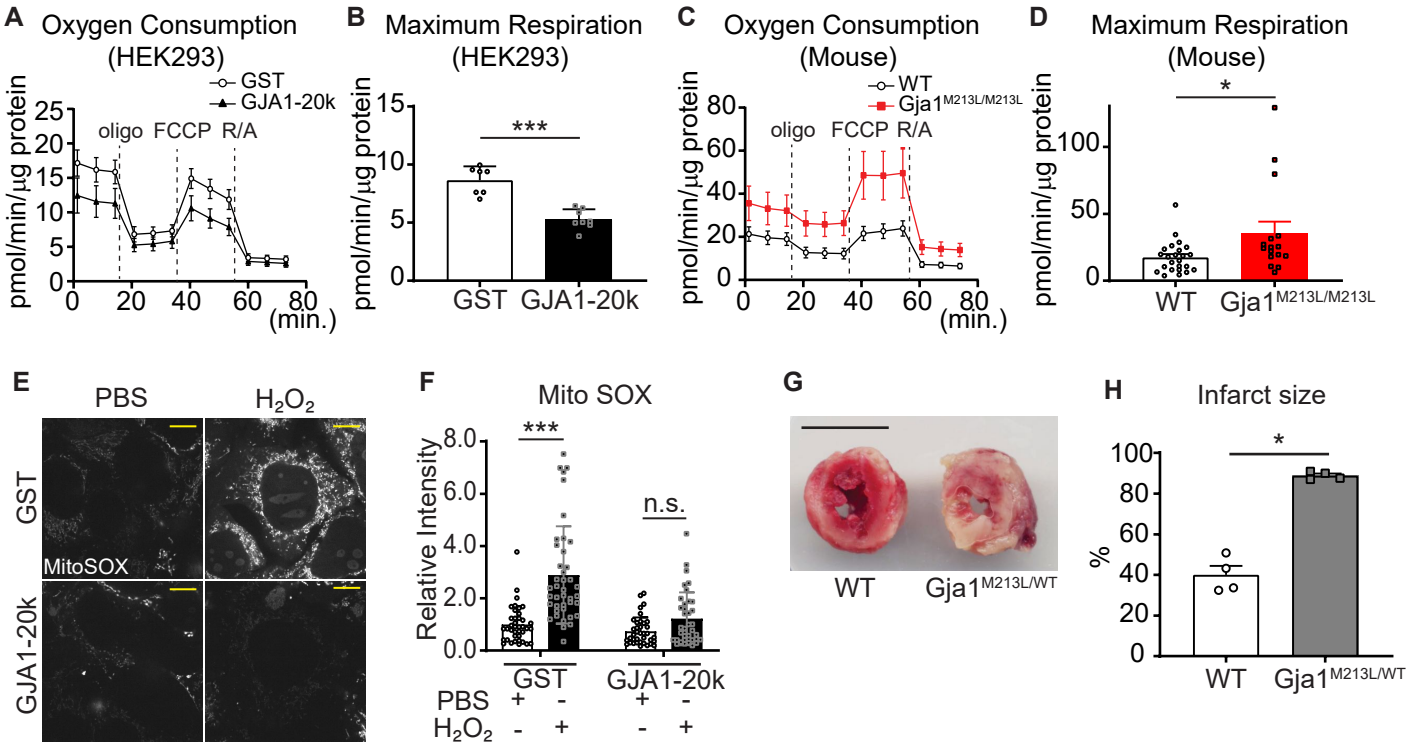


**Figure 5. Mitochondrial metabolic function is preserved by GJA1-20k**

(**A**)–(**D**) Real-time change in OCR by Seahorse assay and the maximum respiration in HEK293 cells (**A** and **B**) and mouse neonatal CM (**C** and **D**). 7 (GST) or 8 (GJA1-20k) replicates from HEK293 cells; n = 24 (WT from 4 hearts) or 16 (Gja1$^{M213L/M213L}$ from 3 hearts) replicates. (**E**) Representative live cell images of MitoSOX with or without $H_2O_2$ treatment to GST- or GJA1-20k-transfected HEK293 cells. (**F**) Relative intensity of MitoSOX. n = 39 (GST, PBS), 41 (GST, H2O2), or 37 (GJA1-20k, PBS or H2O2) cells from three independent experiments. (**G**) Representative images of TTC stained hearts from WT and Gja1$^{M213L/WT}$ mice after I/R. (**H**) Quantification of infarct size after I/R. n = 4. Graphs were expressed as mean ± SD (HEK293) or SEM (mouse). p values were determined by two-tailed Mann-Whitney U-test or two-way ANOVA with Bonferroni's post-hoc test. *p < 0.05, ***p < 0.001; n.s., not significant. Scale bars, 10 µm (**E**); 5 mm (**G**). Exact p values and statistical data are provided in the source data.

Figure 6

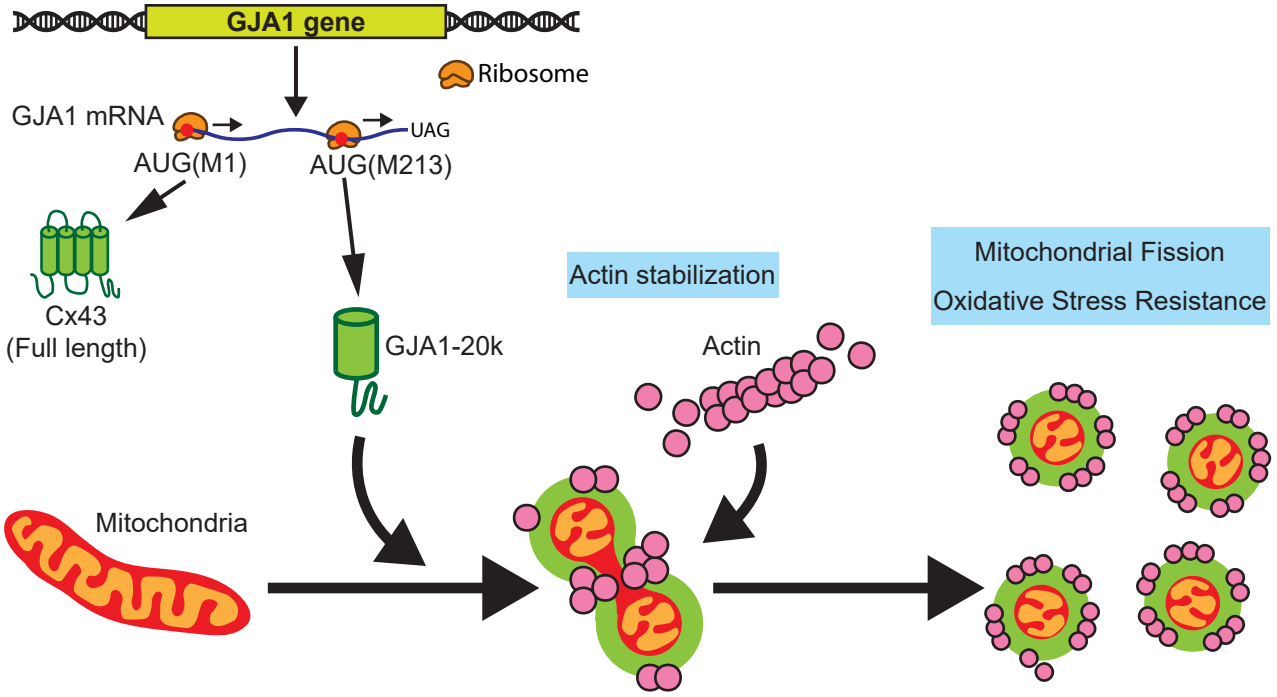


**Figure 6. Schematic summary**

GJA1-20k, internally translated from Gja1 mRNA, localizes mitochondria membrane, stabilizes actin cytoskeleton, and recruits actin around mitochondria to both induce mitochondrial fission and achieve oxidative stress resistance.

# Figure 1—figure supplement 1

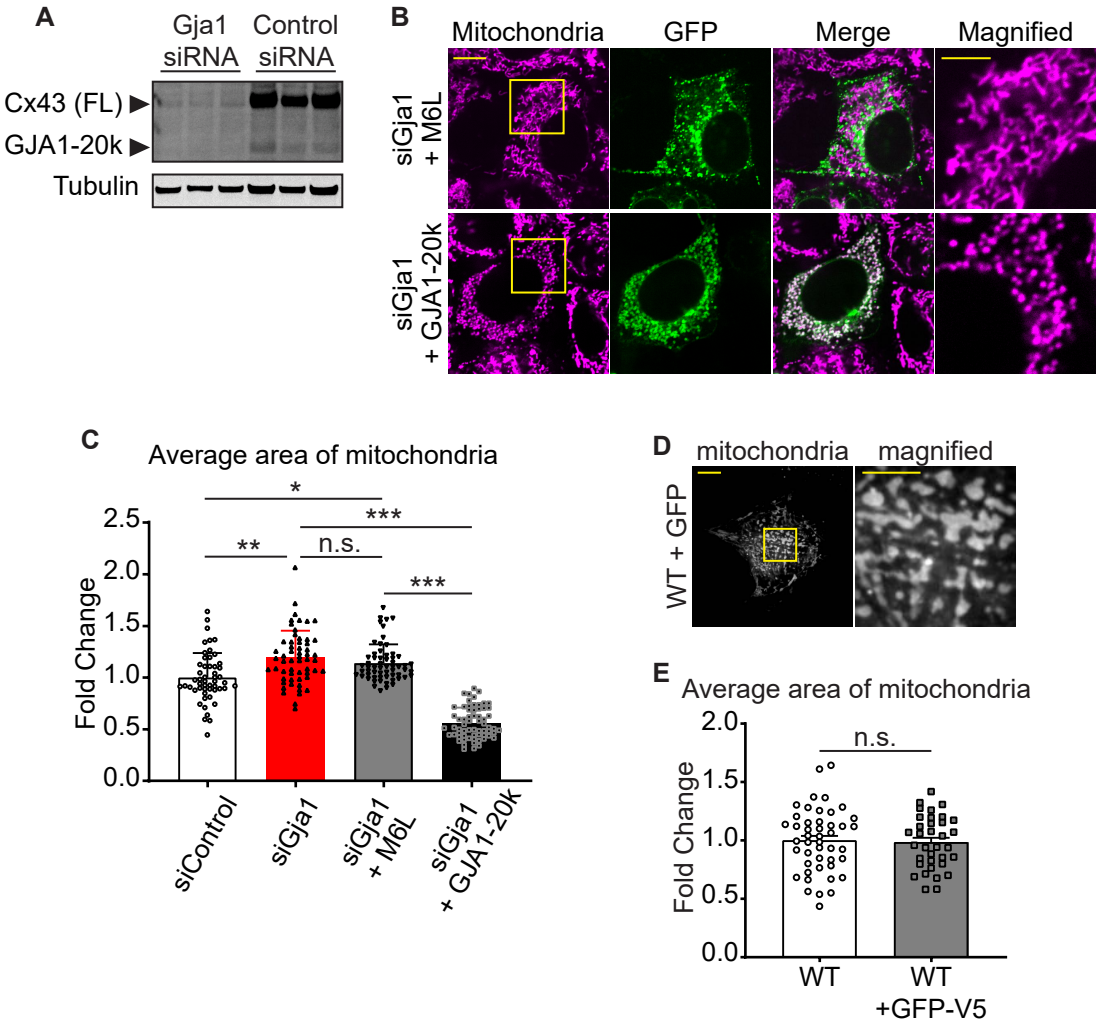


**The confirmation of Gja1 knock-down and the mitochondrial morphology rescued by GJA1-20k**

(**A**) Western blot analysis for Gja1 knock-down by siRNA. Tubulin was used as internal loading control. n = 3 independent experimental repeats. (**B**) The representative confocal live cell imaging of Gja1 knocked-down HEK293 cells with Cx43-M6L or GJA1-20k transfection. (**C**) The fold change in the average area of individual mitochondria. n = 52 (Control), 57 (siGja1), 60 (siGja1 + M6L), or 64 (siGja1 + GJA1-20k) cells from five independent experiments. The images and the values of Control and siGja1 are also shown in Figure 1. (**D**) The representative live cell imaging of mitochondria in WT mouse neonatal CMs with adenovirus-mediated GFP induction. The right panel indicates magnified image surrounded by square. (**E**) The fold change in the average area of individual mitochondria between WT (no virus introduction, the image and the value shown in Figure 1) and GFP-V5 introduction. n = 46 (WT) or 35 (GFP) cells from 4 hearts. Graphs were expressed as mean ± SD (**C**) or SEM (**E**). p values were determined by two-tailed Mann-Whitney U-test or Kruskal-Wallis test with Dunn's post-hoc test. *p < 0.05, **p < 0.01, ***p < 0.001; n.s., not significant. Scale bars, 10 μm or 5 μm in magnified image. Exact p values and statistical data are provided in the source data.

# Figure 2—figure supplement 1

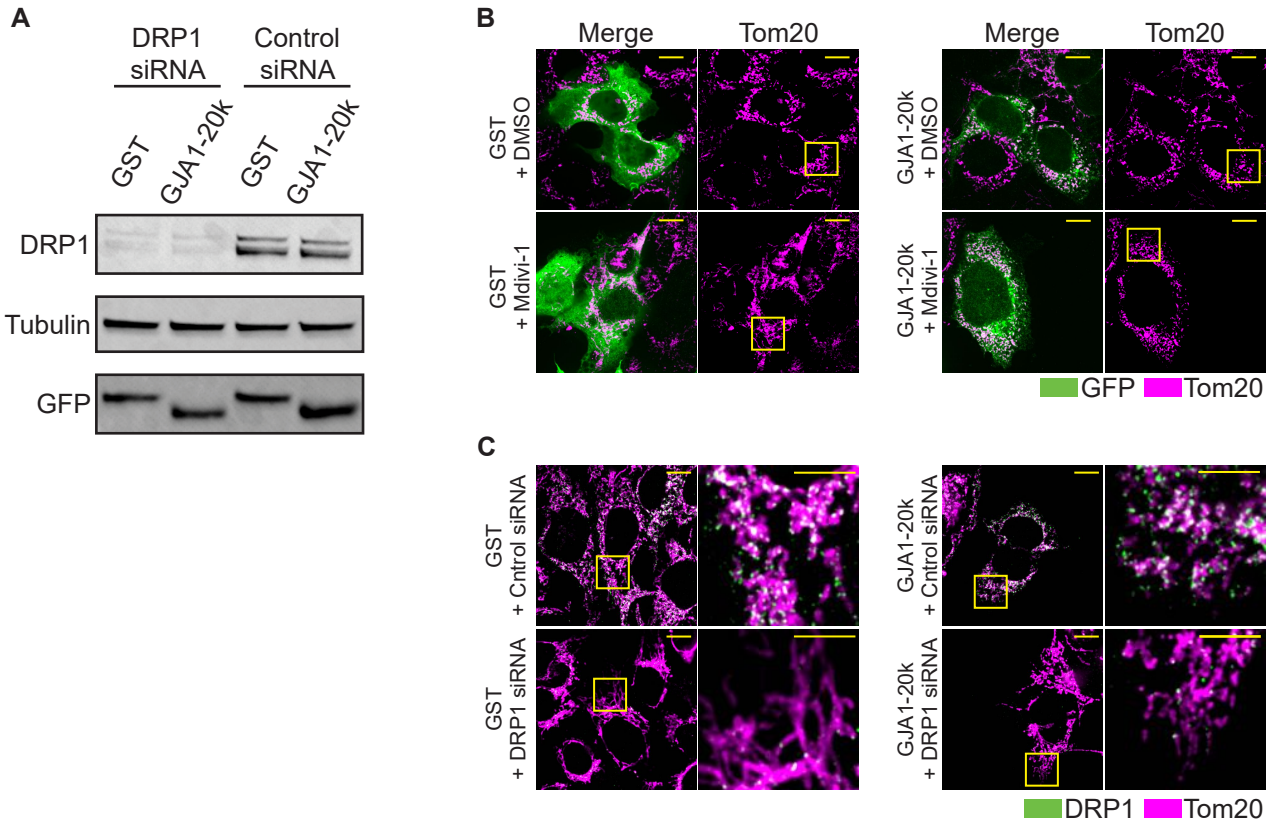


**The confirmation of DRP1 knock-down by siRNA and the mitochondrial morphology rescued by GJA1-20k** (**A**) Western blot analysis for DRP1 knock-down by siRNA. n = 3 independent experimental repeats. (**B**) and (**C**) The representative fixed cell images of mitochondria (visualized by Tom20) with or without Mdivi-1 (**B**), or siDRP1 (**C**) treatment. The magnified mitochondria images surrounded by the square are used in Figure 2. Scale bars, 10 μm (**B** and **C**) or 5 μm in magnified image (**C**).

# Figure 5—figure supplement 1

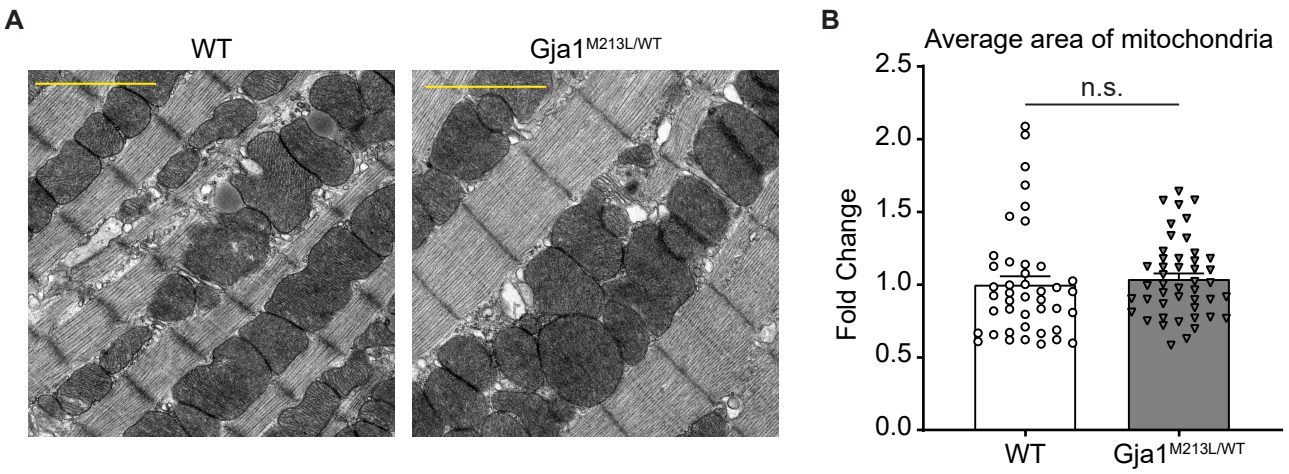


**The mitochondria size did not change in adult mouse heart between WT and heterozygous Gja1$^{M213L/WT}$**
(**A**) The representative electron microscope images from adult mouse hearts (WT or Gja1$^{M213L/WT}$). Scale bars, 2 μm. (**B**) The fold change in the average area of individual mitochondria. n = 43 (WT) or 46 (Gja1$^{M213L/WT}$) images from 3 hearts. Graph was expressed as mean ± SEM. p value was determined by two-tailed Mann-Whitney U-test. n.s., not significant. Exact p values and statistical data are provided in the source data.